HyUSPRe

Hydrogen **U**nderground **S**torage in **P**orous **Re**servoirs

Hydrogen reservoir flow behaviour: Measurements of molecular diffusion, mechanical dispersion and relative permeability

Prepared by: Julia Michelsen, Clausthal Technical University
Eike Marie Thaysen, University of Edinburgh
Sebastian Hogeweg, Clausthal Technical University
Birger Hagemann, Clausthal Technical University
Aliakbar Hassanpouryouzband, University of Edinburgh
Nils Langanke, Clausthal Technical University
Katriona Edlmann, University of Edinburgh
Leonhard Ganzer, Clausthal Technical University

Please cite this report as: Michelsen, J., Thaysen, E.M., Hogeweg, S., Hagemann, B., Hassanpouryouzband, A., Langanke, N., Edlmann, K., Ganzer, L. 2023: Hydrogen reservoir flow behaviour: Measurements of molecular diffusion, mechanical dispersion and relative permeability, H2020 HyUSPRe project report, 67 pp.

This report represents HyUSPRe project deliverable number D4.4.

The HyUSPRe consortium

Funded by

Co-funded by the European Union

Acknowledgement

This project has received funding from the Fuel Cells and Hydrogen 2 Joint Undertaking (now Clean Hydrogen Partnership) under grant agreement No 101006632. This Joint Undertaking receives support from the European Union's Horizon 2020 research and innovation programme, Hydrogen Europe and Hydrogen Europe Research.

Disclaimer

This document reflects the views of the author(s) and does not necessarily reflect the views or policy of the European Commission. Whilst efforts have been made to ensure the accuracy and completeness of this document, the HyUSPRe consortium shall not be liable for any errors or omissions, however caused.

Executive summary

The transition to zero-carbon energy generation from renewable sources requires storing renewable energy intermittently in the form of energy carriers such as hydrogen (H_2) to overcome imbalances between renewable energy supply and energy demand. Large-scale subsurface storage of H_2 in porous media, e.g. in globally abundant depleted gas fields and saline aquifers, is being considered as an alternative to expensive purpose-built storage containers above ground. However, since hydrogen and natural gas differ in their properties, a particular attention should be given to the flow behaviour of hydrogen.

This report summarizes the properties of H_2 under subsurface storage conditions, outlines the current state of the art on H_2 flow in porous media, followed by a description of experimental studies that characterize the H_2 fluid flow behaviour in porous media. The first experimental series investigated the molecular diffusion for a binary H_2-CH_4 system in different reservoir rocks. Based on the measurement results effective diffusion coefficients were determined. The second experimental series investigated the mechanical dispersion also for a H_2-CH_4 system. Here, longitudinal dispersivities were determined. The measurements of molecular diffusion and mechanical dispersion were both conducted at a range of temperatures and pressures to investigate the effects of the two parameters (temperature and pressure) on diffusive and dispersive mixing. The next study investigated unsteady state drainage H_2/brine relative permeabilities as affected by variations in sample mineralogy and pore structure, as well as variations in pressure and pore fluid salinity, where the applied ranges in the latter two parameters are selected to be representative of potential geological storage sites. The final study outlines the effect of pore fluid pressure on H_2 injectivity and recovery.

In total 29 measurements of molecular diffusion were performed and interpreted. The influence of pressure, temperature and water saturation was investigated using a Bentheimer sandstone as reference sample. The determined effective gaseous diffusion coefficients varied between $5 \cdot 10^{-9}$ and $2.3 \cdot 10^{-7}$ m²/s. The results showed clear trends, but deviations were observed from conventional correlations at pressures above 75 bar and for the dependence on temperature at 100 bar. The decreasing trend of effective diffusion coefficient with increasing water saturation fits the expectation. The comparison of effective diffusion coefficients for different samples at reference conditions indicated that the effective diffusivity increases with porosity and permeability.

For the mechanical dispersivities 13 measurements were carried out. The measurements investigated the effects of pressure, temperature and flow velocity on dispersivity. The interpreted longitudinal mechanical dispersivity was between 0.018 and 0.060 m. The results showed that dispersivity is not independent of these parameters, indicating that fluid properties such as density and viscosity play a role. However, Scheidegger's theory for dispersion was found to sufficiently predict dispersive mixing between two gases under subsurface storage conditions. Nevertheless, the study also suggests that this theory may not capture all effects, and the strong sensitivity to pressure highlights the need for further investigation into the relationship between fluid properties and dispersivity.

The experiments showed that relative permeability of hydrogen is influenced by pore structure and porosity, with increasing porosity resulting in increased relative permeability. When pressure is increased at higher hydrogen saturations, the viscosity of hydrogen increases, which reduces its relative permeability. Salinity also has an effect on relative permeability, with an increase in salinity causing a reduction in relative permeability, possibly due to an increase in interfacial tension. All relative permeability curves on three different samples exhibit a strongly water-wet behavior.
The experimental results are analysed and processed to be used in numerical simulations to forecast future storage operations.

About HyUSPRe

Hydrogen **U**nderground **S**torage in **P**orous **Re**servoirs

The HyUSPRe project researches the feasibility and potential of implementing large-scale underground geological storage for renewable hydrogen in Europe. This includes the identification of suitable porous reservoirs for hydrogen storage, and technical and economic assessments of the feasibility of implementing large-scale storage in these reservoirs to support the European energy transition to net zero emissions by 2050. The project will address specific technical issues and risks regarding storage in porous reservoirs and conduct an economic analysis to facilitate the decision-making process regarding the development of a portfolio of potential field pilots. A techno-economic assessment, accompanied by environmental, social, and regulatory perspectives on implementation will allow for the development of a roadmap for widespread hydrogen storage by 2050, indicating the role of large-scale hydrogen storage in achieving a zero-emissions energy system in the EU by 2050.

This project has two specific objectives. Objective 1 concerns the assessment of the technical feasibility, associated risks, and the potential of large-scale underground hydrogen storage in porous reservoirs for Europe. HyUSPRe will establish the important geochemical, microbiological, flow, and transport processes in porous reservoirs in the presence of hydrogen via a combination of laboratory-scale experiments and integrated modelling; and establish more accurate cost estimates to identify the potential business case for hydrogen storage in porous reservoirs. Suitable storage sites will be identified, and their hydrogen storage potential will be assessed. Objective 2 concerns the development of a roadmap for the deployment of geological hydrogen storage up to 2050. The proximity of storage sites to large renewable energy infrastructure and the amount of renewable energy that can be buffered versus time varying demands will be evaluated. This will form a basis for developing future scenario roadmaps and preparing for demonstrations.

Document information, revision history, approval status

Document information

Title:	Hydrogen reservoir flow behaviour: Measurements of molecular diffusion, mechanical dispersion and relative permeability
Lead beneficiary:	Clausthal Technical University
Contributing beneficiaries:	University of Edinburgh
Due date:	2023.03.31
Dissemination level:	Public
Published where:	HyUSPRe website
Recommended citation:	Michelsen, J., Thaysen, E.M., Hogeweg, S., Hagemann, B., Hassanpouryouzband, A., Langanke, N., Edlmann, K., Ganzer, L. 2023: Hydrogen reservoir flow behaviour: Measurements of molecular diffusion, mechanical dispersion and relative permeability, H2020 HyUSPRe project report, 67 pp.

Revision history

Version	Name	Delivery date	Summary of changes
V01	Thaysen, E.M.	2022.10.5	Draft delivered for internal review
V02	Hagemann, B.	2023.03.06	Finalized draft for review
V03	Hagemann, B.	2023.03.30	Finalized report after review
V04	Cremer, H.	2023.03.31	Final layouted version

Approval status

Role	Name	Delivery date
Deliverable responsible:	Clausthal University of Technology	2023.03.30
Task leader:	Birger Hagemann, Katriona Edlmann	2023.03.30
WP leader:	Birger Hagemann	2023.03.30
HyUSPRe lead scientist	Remco Groenenberg	2023.03.31
HyUSPRe consortium manager:	Holger Cremer	2023.03.31

Table of Content

1 Introduction

Over the course of the ongoing energy transition, underground energy storage is expected to become increasingly important to manage the fluctuations in the production of renewable energy from wind and solar. Underground hydrogen storage (UHS) in porous reservoirs in the subsurface is a new technology that can help to transition to a low carbon society and mitigate climate change. Several knowledge gaps have been identified that must be addressed to enable the implementation of hydrogen storage in porous media. One particular area of uncertainty is the H_2 fluid flow behaviour in porous media, which determines the hydrogen recovery, thereby ultimately affecting the economic feasibility of the storage operation. For underground hydrogen storage the mixing behaviour of the injected hydrogen and residual natural gas, which is mainly methane, in porous reservoirs plays an important role. The mixing of the gases is mostly influenced by the two processes molecular diffusion and mechanical dispersion (Figure 1). Molecular diffusion is a mixing process that is driven by concentration gradients, whereas mechanical dispersion is caused by the movement of fluids through the pore space. For underground storage in aquifers the effects of viscous fingering and lateral spreading should be taken into account. Another important aspect for UHS besides the mixing behaviour of hydrogen and the initial gas is the immiscible gas-liquid interaction of hydrogen and brine, where relative permeability is of special importance. The relative permeability of a phase describes the ratio of the effective permeability of that phase to the absolute permeability. In our case it is important to know the relative permeability of H_2 in the presence of other fluid phases (typically brine).

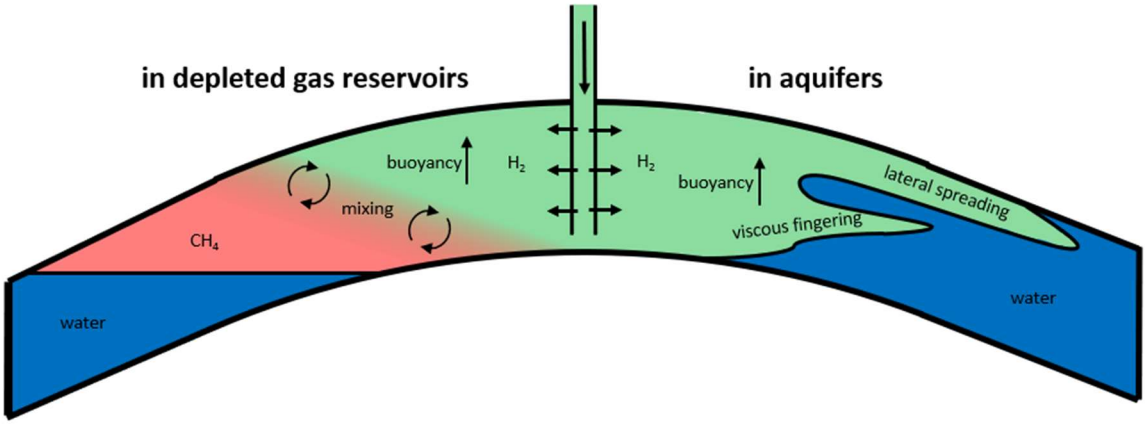

Figure 1. Sketch of gas mixing and hydrodynamic effects in an underground hydrogen storage.

The aim of this work package (WP4) was to investigate the flow behaviour of hydrogen in a porous reservoir with laboratory experiments concerning the molecular diffusion, mechanical dispersion as well as the hydrogen/brine relative permeability. Besides the experimental measurements the processing of the experimental data for the use in numerical models was also part of this WP.

2 State of the art

2.1 Fluid flow properties of the hydrogen compared to methane, nitrogen and carbon dioxide

The injection of gas containing higher percentages of hydrogen influences thermodynamic properties, impacting the volumetrics and energy densities of stored fluids, but also the transport process is affected remarkably. Hydrogen, as the lightest chemical element overall, comes with low viscosity and less compressibility than most other gases. An example of the trend of compressibility (z-factor) and viscosity versus pressure in comparison to relevant natural gas components is depicted in Figure 2. While for most gases, the z-factor at increased pressures is below one, yielding increased compressibility, the compressibility of hydrogen worsens with increasing pressure. In terms of viscosity, hydrogen comes up with the lowest values and is approximately 1-1.5 times smaller than methane. While the density mainly impact phenomena such as gravity override, the viscosity will lead to unstable displacements characterized by viscous fingering. Also, differences in interfacial tension yielding relative permeability curves could alter the two-phase displacement further. The mixing of the components in the gas phase (e.g. with the cushion gas) is strongly governed by molecular diffusion and mechanical dispersion. These effects and the current state of research are elucidated in the following subsections.

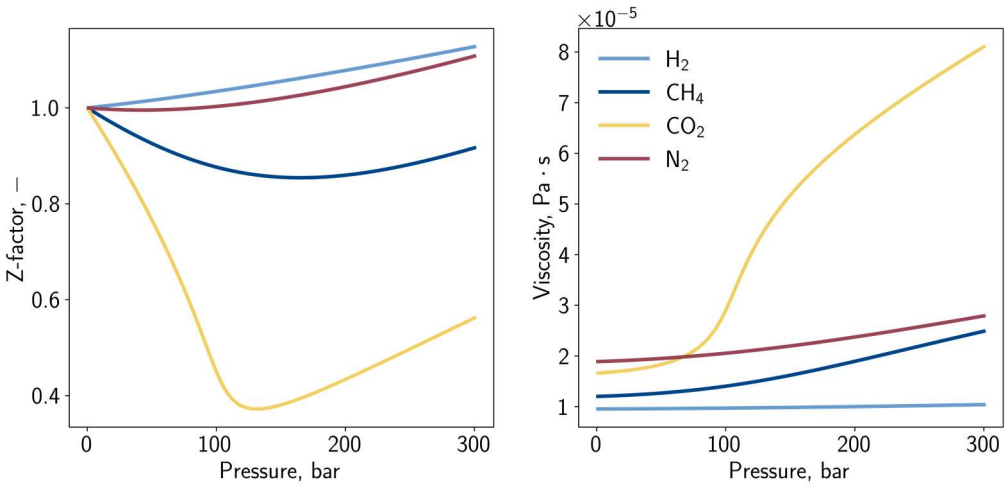

Figure 2. Z-factor and viscosity versus pressure at a temperature of T=50°C; The compressibility is modelled based on the Peng and Robinson EoS (Peng and Robinson, 1976) , and the dynamic viscosity is based on a combination of the Stiel and Thodos and Lohrenz correlations (Stiel and Thodos, 1961; Lohrenz et al., 1964).

2.2 Gas mixing in underground gas storage

The mixing of gases in porous reservoirs plays an important role for the operation of an underground storage site. Knowledge about the mixing behaviour is particularly relevant for the estimation of the injection and withdrawal performance in an underground storage as well as for the recoverability of the stored hydrogen from the porous reservoir. There are two major mechanisms which are causing the mixing of miscible gases. On the one hand it is convective flow, on the other hand it is the gas transport by diffusive and dispersive processes. The convective flow is influenced by gravity, viscosity, capillarity and compressibility (Tek, 1989).

The relationship between molecular diffusion and mechanical dispersion in porous media in dependence on the flow velocity is shown in Figure 3. In case of low flow velocities the mixing process is dominated by molecular diffusion, whereas higher velocities lead to a dispersive controlled transport. The transient region in between is influenced by both processes.

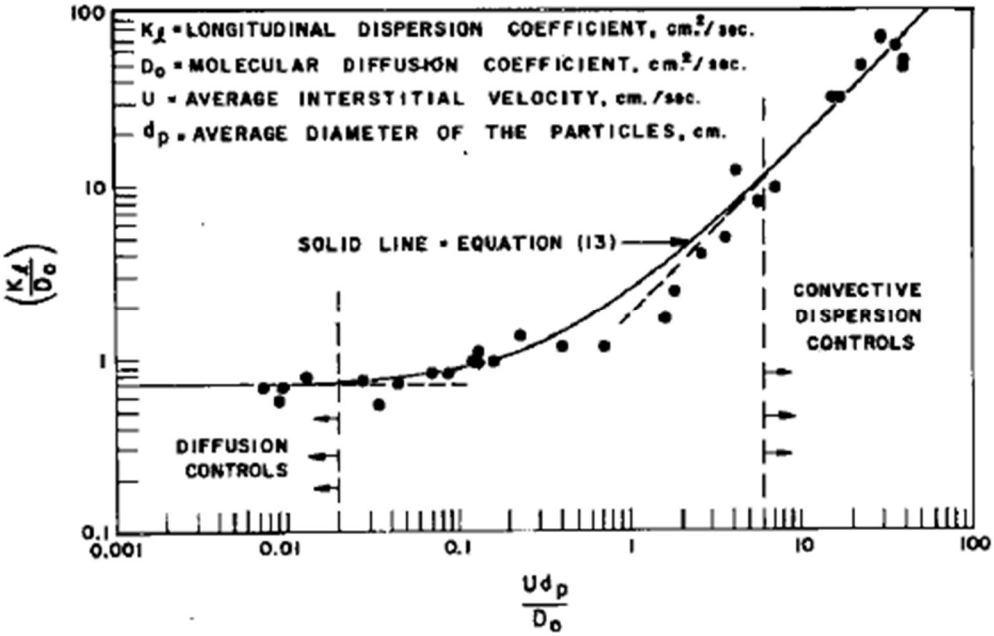

Figure 3. Diffusive and dispersive mixing regimes in porous media flow (Perkins and Johnston, 1963).

2.3 Molecular diffusion of hydrogen in the gas phase

Diffusion is a physical process that is driven by concentration differences and thus can occur even without pressure differences. It can take place under both stationary and unsteady conditions. The difference between the two conditions is that stationary diffusion occurs at a constant rate, while the unsteady diffusion rate is a function of time. Both diffusion conditions can be described using Fick's laws and can be used to measure the diffusion coefficient. Fick's first law states that the diffusion flux is directly proportional to the concentration gradient (Ho and Webb, 2006).

In a porous medium the diffusivity is usually reduced compared to the free gaseous diffusivity because the gas has less space and must travel a longer distance through it. Factors which are influencing the effective diffusivity are porosity, tortuosity and the presence of other fluid phases in the pore space. For binary systems the diffusive flux of gas components in a porous medium can be described by the following relation:

$$J_{\text{diff}}^{k} = -\rho D_{\text{eff}} \nabla c^{k}$$

where J_{diff}^{k} is the diffusive flux of component k in mol/m²/s, ρ is the molar density of gas in mol/m³, D_{eff} is the binary effective diffusion coefficient in m²/s and ∇c^{k} is the gradient of the mole fraction of component k.

Knudsen diffusion occurs when the mean free path of the gas molecules is comparable to or larger than the pore sizes of the porous medium. As a result, the molecules collide more

frequently with the pore walls than with each other. Knudsen diffusion can be characterized by the Knudsen number, K_n. A Knudsen number greater than 10 indicates Knudsen diffusion. In this case, collisions between molecules and the pore wall are dominating. To find out if Knudsen diffusion is an issue in the experiments which are carried out within this working package, the Knudsen number is calculated by using the following equation (Bear, 2018):

$$K_n = \frac{\lambda}{l_{pm}}$$

λ is the mean free path of the molecules in m and l_{pm} is the characteristic length dimension of the void space, here the pore diameter, in m. When assuming a mean free path of $6.6 \cdot 10^{-8}$ m and a mean pore diameter of $5 \cdot 10^{-5}$ m for a Bentheimer sandstone, which is one of the samples used for the measurements, the Knudsen number is $1.32 \cdot 10^{-3}$. Consequently, Knudsen diffusion does not play a role in the measurements here.

Various apparatuses and methods have been developed to measure molecular diffusion through porous materials. The Wicke-Kallenbach method is performed under stationary conditions (Ho and Webb, 2006; Soukup et al., 2008). In this method, a diffusion cell consisting of two chambers separated by a porous sample is used. Two gases are used for the measurement. One gas flows continuously through one chamber, and the other through the opposite chamber. Throughout the measurement, the pressure in both chambers is kept constant. The gas compositions in both chambers are continuously analyzed by gas chromatography.

Another method for diffusion measurement is the Graham cell. The setup of this measurement method is similar to that of the Wicke-Kallenbach method (Soukup et al., 2008). Again, two gases flow continuously through the two chambers and the porous medium until a steady state of diffusion is reached. Then, the inflow and outflow at one side are closed so that the diffusive volume flow can be determined using a flow meter. Unlike the Wicke-Kallenbach method, it is not necessary to continuously analyze and monitor the outflowing gas from both chambers in this method.

Chen et al. (1977) and Pandey et al. (1974) both performed diffusion experiments with porous samples using a modified Wicke-Kallenbach set-up. In addition, Guevara-Carrion et al. (2019) investigated diffusion of CH_4 in supercritical CO_2 under increased pressure but without a porous medium. Diffusion measurements found in literature and their results are listed in Table 1.

Table 1. Diffusion measurements in literature.

Reference	Used gases	T [°C]	P [bar]	Method	Material	Diffusion coefficient [m²/s]
Pandey et al. (1974)	He, N_2	24 - 42	1 - 5	Steady state flow (for dry samples), unsteady-state flow (for low permability and water-saturated samples)	Rock samples	Steady state: $2.14 \cdot 10^{-6}$ to $1.19 \cdot 10^{-4}$ Unsteady state: $1.67 \cdot 10^{-8}$ to $1.88 \cdot 10^{-5}$ (only dry samples considered)
Chen et al. (1977)	CH_4, N_2	35	1	Steady state flow (modified Wicke-Kallenbach)	Rock samples	$2.59 \cdot 10^{-5}$ to $2.00 \cdot 10^{-3}$ (only dry samples considered)
Guevara-Carrion et al. (2019)	CH_4, CO_2	19.4 – 59.7	90 - 147	Taylor set-up	Bulk	$1.46 \cdot 10^{-8}$ to $3.70 \cdot 10^{-8}$

2.4 Gas mixing by mechanical dispersion

Mechanical dispersion is a mixing process of fluids due to their movement and current in porous media. Dispersion is driven by variations in the flow velocity which can occur on different scales. These variations are mainly caused by the pore-size distribution, tortuosity and heterogeneity of the porous medium. On microscopic scale larger pores and pore throats lead to higher velocities than smaller pores. In addition, the non-uniform velocity profile along the pore cross-section induces velocity variations (Ho and Webb, 2006).

The effect has to be introduced into macroscale models to compensate the error made by the assumption of an averaged Darcy velocity. Consequently, this effect arises during the upscaling to a representative elementary volume (REV).

Mechanical dispersion can be described by assuming a linear relation to the flow velocity (Scheidegger, 1961):

$$J_{\text{disp}}^{k} = -\rho \alpha U \nabla c^{k}$$

where J_{disp}^{k} is the dispersive flux of component k in mol/m²/s, ρ is the molar density of gas in mol/m³, α is the mechanical dispersivity in m, U is the true flow velocity in m/s and ∇c^{k} is the gradient of the mole fraction of component k in 1/m.

Information about the dispersion measurements in literature is summarized in Table 2. Mohammed et al. (2019) conducted core flooding experiments for the dispersion measurement of N_2,CO_2 and CH_4 in a core sample. In the study by Yang et al. (2023) hydrogen dispersion in Berea sandstone samples was measured in core flooding experiments. Carriere et al. (1985) and Laille et al. (1986) investigated the mixing behaviour of gases in porous reservoirs with tracer tests in the field.

Table 2. Dispersion measurements in literature.

Reference	Used gases	T [°C]	P [bar]	Method	Material	Dispersivity [m]
Carriere et al. (1985)	H_2 tracer with natural gas	N/A	N/A	Field test	Porous reservoir	2
Laille et al. (1986)	H_2 tracer with natural gas	N/A	N/A	Field test	Porous reservoir	25
Kurihara et al. (2000)	CH_4, Ar	N/A	N/A	Slimtube displacement	Glass beads	$1.20 \cdot 10^{-2}$
Mohammed et al. (2019)	N_2, CO_2, CH_4	35-40	103.42	Unsteady state displacement, core flooding	Bandera grey sandstone sample	$6.37 \cdot 10^{-4}$
Yang et al. (2023)	H_2, N_2	N/A	50	Core flooding, NMR	Berea sandstone	$3.10 \cdot 10^{-4}$

2.5 Hydrogen relative permeability

At the time of writing only three studies on the H_2 relative permeability exist. Yekta et al. (2018) performed steady-state experiments on Vosges sandstones at two pressure/temperature conditions (55 Bar and 20 °C, and 100 Bar and 45 °C), representing a shallow aquifer and a deep aquifer, respectively. Measurements of the relative permeability were after drainage, only, and showed little effect of the experimental condition on the max. initial saturation (S_{nwi}) of H_2 (H_2 S_{nwi} : 59-60 %) and H_2 relative permeability, K_{rH2} (0.03492-0.04404) (Yekta et al., 2018).
Boon and Hajibeygi, (2022) derived steady-state relative permeability curves in Berea sandstone for both drainage and imbibition at 18 °C and 100 Bar. Hydrogen relative permeabilities during drainage at maximum H_2 S_{nwi} of ~50 % were ~0.09 for both drainage and imbibition but there was significant hysteresis in the relative permeability measurement at lower H_2 saturations due to capillary trapping of H_2 during imbibition (Boon and Hajibeygi, 2022). Lysyy et al. (2022b) who used the steady state technique to measure primary drainage, imbibition and secondary drainage K_{rH2} at 30 Bar and 30°C in Berea sandstone, confirmed the finding of hysteresis in the K_{rH2}. Hydrogen relative permeabilities during drainage at maximum H_2 S_{nwi} of ~65 % were ~0.07 (Lysyy et al., 2022b). The authors also found that K_{rH2} was significantly different from N_2 relative permeability (Lysyy et al., 2022b).

2.6 Hydrogen injectivity and recovery in porous media

At the time of writing two X-ray computed micro-CT studies, one micro-model study and one nuclear magnetic resonance (NMR) study on H_2 injectivity and recovery exist. (Al-Yaseri et al., 2022) used NMR to find S_{nwi} and S_{nwr} of H_2 of 4 % and <2 %, respectively, in a Fontainebleau sandstone at 0.4 MPa and ambient temperature. Jha et al. (2021) conducted a single cycle H_2-brine displacement sequence in a 5 mm diameter and 15 mm length core of Gosford sandstone, and used µCT to calculate S_{nwi} of H_2 of 65 % during drainage and S_{nwr} of H_2 of 41 %. The rock sample in Jha et al. (2021) was sufficiently short for capillary end effects to dominate the flow behaviour, where the wetting phase accumulates close to the production face of the core (Pak et al., 2015). In addition, the experiments by Jha et al. (2021) and Al-

Yaseri et al. (2022) were performed at ambient pressure and very low pressure, respectively, leaving open the question of variations in H_2 wetting and flow behaviour at reservoir conditions (Iglauer et al., 2021). The effect of increases in capillary number (N_C) from 7.7×10^{-7} to $3.8 \times 10^{--4}$ on the H_2 flow through a sandstone micro-model at 0.5 MPa was investigated by Lysyy et al. (2022a) who found that the S_{nwi} of H_2 increased correspondingly from 18 % to 79 %. Recently, Jangda et al. (2022) reported S_{nwi} of H_2 and S_{nwr} of H_2 of 36 % and 20-25 %, respectively in unaged Bentheimer sandstone at 10 MPa and 50 °C. The authors found higher recovery of H_2 for non-H_2-equilibrated brine compared to that of H_2-equilibrated brine (43.1 % vs. 31.6 %, respectively) (Jangda et al., 2022), suggesting dissolution of H_2.

3 Measurement of molecular diffusion coefficients

3.1 Experimental setup and procedure

The measurement of molecular diffusion is performed with a binary diffusion setup at Clausthal University of Technology. The diffusion measurement method was modified after Wicke and Kallenbach (1941). The main component of the setup is a core holder, which is designed for rock samples with a length of up to 6 cm and a diameter of 3 cm, as shown in Figure 4.

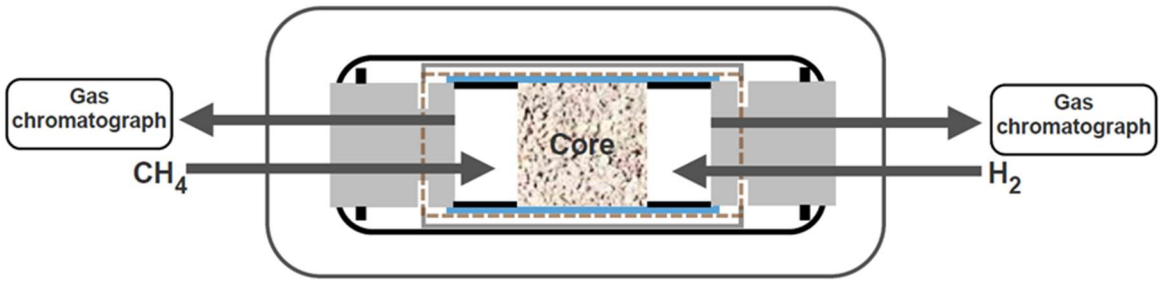

Figure 4. Sketch of the core holder.

The rock sample, two hollow cylinders, two targets and two end pieces are first installed in a Viton sleeve and then in the core holder.

When a low diffusion rate is expected, a stationary method is used. Here, both hollow cylinders, which work as chambers, have the same volume. During the diffusion measurement the chambers are flooded with the sample gases, on the left side with methane and on the right side with hydrogen. The injection of the gases is controlled by high-pressure syringe pumps which are regulating gas filled floating piston chambers. The pressure in the chambers are regulated by pressure regulators, which are connected to the chamber outlets. Behind the left back pressure regulator, the composition of the outflowing gas is constantly analysed by a micro gas chromatograph.

For measurements with higher diffusion rates a quasi-stationary method is used. In this method one chamber contains a much larger volume than the other one. The large chamber must have a multiple of the volume in relation to the pore volume of the rock sample. The large chamber has one inlet. Prior to the measurement the chamber is filled with hydrogen gas and pressurised. On the other side of the sample is the target, which has one inlet and one outlet. During the experiment methane is injected into the cell via this inlet. The injection is again controlled by a syringe pump, which drives a floating piston chamber. This floating piston chamber is filled with methane. At the outlet of the target there is a backpressure regulator installed, which regulates the pressure in the diffusion cell to a constant value during the measurement. Behind the backpressure regulator again a gas chromatograph analyses the composition of the outflowing gas continuously. A sketch of the complete experimental setup for both configurations is shown in Figure 5.

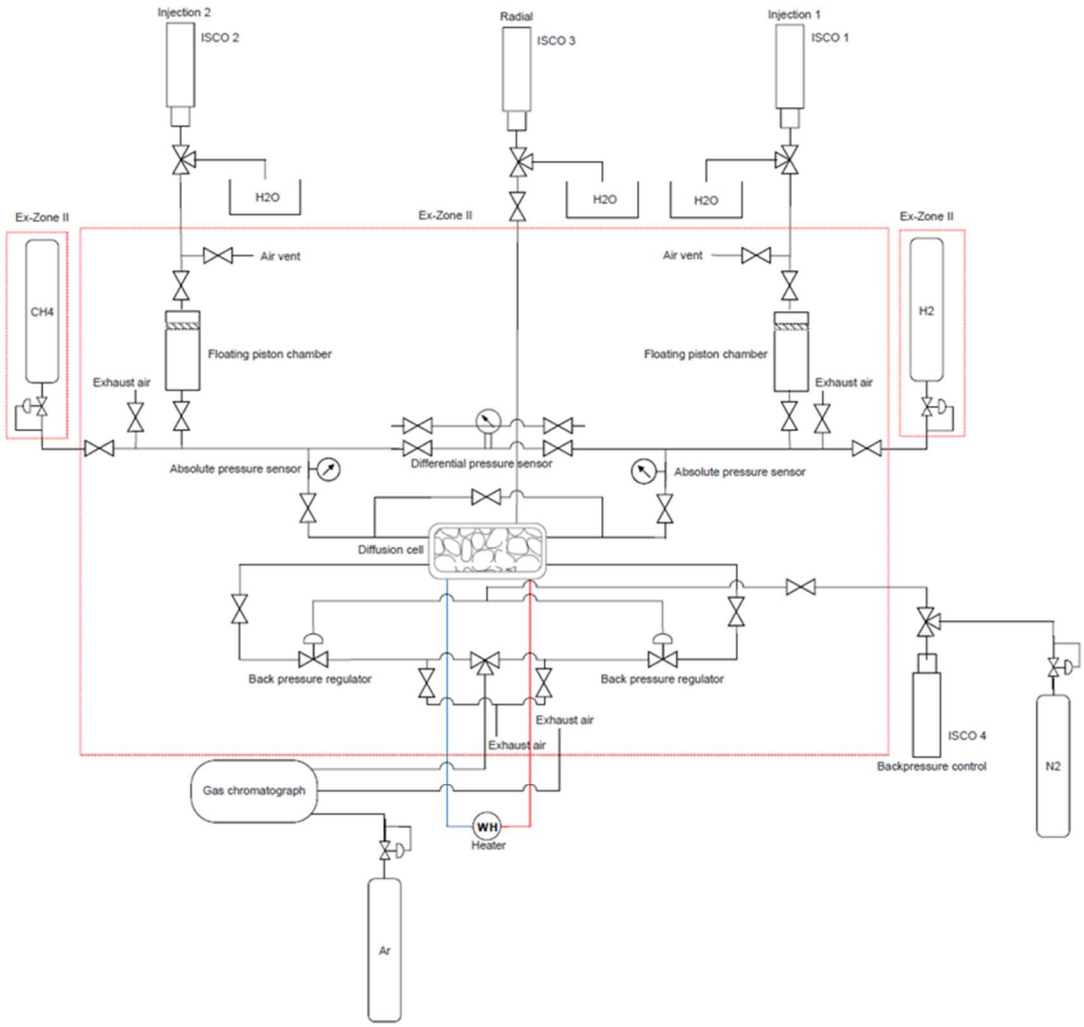

Figure 5. Sketch of the experimental setup for diffusion measurement.

The measurement of an effective diffusion coefficient is performed using the following four steps:

1. Sample installation: The cylindrical sample of the porous material is inserted into a Viton sleeve together with the chambers, targets, and end pieces, and installed in the diffusion measurement cell. The diffusion measurement cell is connected to the measuring device. For the measurement of a water-saturated sample, there is an additional step prior to the installation into the measurement cell. The sample is saturated with distilled water externally under vacuum in a desiccator. The sample was pushed into a Viton sleeve and compressed air was used to displace the water and obtain a residual saturation. The resulting saturation was determined by weighing the sample directly before starting the experiment and afterwards.

2. Leakage test: The radial pressure and the measuring pressure are gradually increased to the desired values. The radial pressure should be 1.5 times or at least 50 bar higher than the measuring pressure. A leak test with nitrogen is carried out for at least 2 hours, during which the leakage rate should be no more than 0.5 % of the later injection rate.

3. Preparation:
   Stationary measurement
   As a first preparation step, the two floating piston chambers are filled with the samples gases (hydrogen and methane). The two chambers are flooded with the sample gases to displace impurities and contamination. One chamber should be filled with >99.9 % hydrogen and the other one with >99.9 % methane. Then both chambers are pressurized up to the measuring pressure.

   Quasi-stationary measurement
   The chambers and the sample are flowed through with hydrogen from a gas cylinder. The purity of the outflowing gas is repeatedly analyzed with the process gas chromatograph. Again a gas purity of over 99.9 % should be ensured. The chambers and sample are then pressurized up to the desired measuring pressure with hydrogen. This is done via a gas booster at higher pressures. The floating piston chamber is filled with methane. Again, a gas purity of over 99.9 % must be ensured, which is achieved through repeated flushing. Filling to the desired measuring pressure is also done via the gas booster.

4. Measurement:
   Stationary measurement
   Injection at a constant rate on both sides is started and the shut-off valves on both sides are opened. The composition of the outflowing gas is continuously analysed with the process gas chromatograph.

   Quasi-stationary measurement
   Injection of methane is started at a constant rate, and the shut-off valve separating the diffusion measurement cell and the floating piston chamber is opened. The composition of the outflowing gas is again analyzed with the process gas chromatograph every three minutes.

3.2 Rock samples

For the diffusion measurements in total seven storage rock samples were selected from the core material provided by the HyUSPRe project partners. Additionally, one Bentheimer sandstone sample from a surface quarry was selected as a reference sample. All used samples and their properties are listed in Table 3. The porosity was measured by a gas pycnometer (micromeritics AccuPyc II 1340) using helium. The permeability was measured in a core flooding cell using nitrogen. The radial pressure during the permeability measurements was 20 bar and the gas pressure approx. 10 bar. As “mean pressure” the arithmetic mean between the minimum and maximum (allowable) operating pressure at reference depth (e.g. mid-point of the reservoir) was defined. Alternatively, for locations which were not used as gas storage before, the mean pressure is defined as $0.75 \cdot p_{\mathrm{init}}$ (initial reservoir pressure).

Table 3. Selected rock samples for the diffusion measurements

Sample site/ formation	Lithology	Porosity [%]	Permeability [mD]	Dry density [g/cm³]	Site conditions	
					Mean pressure [bar]	Temperature [°C]
Bentheimer sandstone	Sandstone	24.7	2500	1.99	-	-
Chattian Sand	Sandstone	29.9	71.0	1.90	106	50
Aquitanian formation	Sandstone	26.8	157.6	1.99	53.5	25
Pliocene Sands	Sandstone	31.7	718.6	1.83	88.3	45
Ebes Fm.	Limestone	19.9	23.6	2.19	140.5	107
Ujfalu Fm. 1	Sandstone	32.1	288.2	1.84	116.5	86
Detfurth formation	Sandstone	27.4	263.1	1.93	287.25	96
Rough Rotliegendes	Sandstone	17.6	17.2	2.20	203	92

3.3 Interpretation and calculation of effective diffusion coefficients

Stationary conditions

For diffusion measurements where steady-state conditions where reached the interpretation and the calculation of effective diffusion coefficients was done according to Chen, Katz and Tek (1977). Based on Fick's first law they derived the following equation:

$$D_e = \frac{N_b Z}{A\left(C_{\text{right}}^{H_2} - C_{\text{left}}^{H_2}\right)}$$

where N_b is the molar rate of H_2 diffusing through the sample in mol/s, Z is the length of the sample in m, A is the cross-sectional area of the sample in m² and C are molar concentrations in mol/m³. The molar density (or total molar concentration) of the gas is calculated under pressure and temperature by using the ideal gas law. For the molar hydrogen concentration this value is multiplied by the mole fraction measured by the gas chromatograph:

$$C^{H_2} = c_g^{H_2} \frac{p}{RT}$$

where $c_g^{H_2}$ is the mole fraction of H_2 in the gas phase, p is the pressure in Pa, R is the universal gas constant in J/K/mol and T is the temperature in K.

Quasi-stationary conditions

Alternatively, a one-dimensional numerical simulation model was used to obtain the effective diffusion coefficient by a model fitting process when steady-state conditions were not reached. A numerical simulation model was implemented in COMSOL Multiphysics. The model solves

the following partial differential equation, which is based on Fick's second law, in a one-dimensional domain (cf. Figure 6):

$$\frac{p}{RT}\phi\frac{\partial c}{\partial t} = \frac{p}{RT}D\frac{\partial^2 c}{\partial x^2}$$

where p is the measurement pressure in Pa, R is the universal gas constant in J/(mol*K), T is the measurement temperature in K, ϕ is the porosity of the sample, c is the molar fraction of hydrogen, D is the effective diffusion coefficient in m²/s.

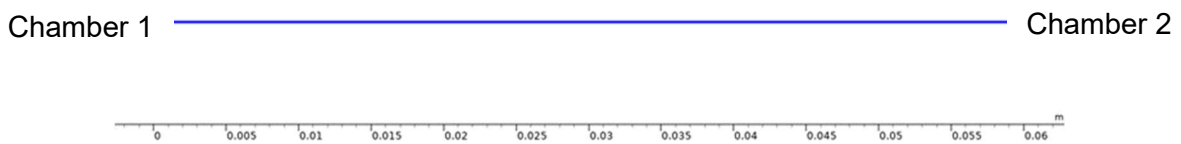

Figure 6. One-dimensional domain for the simulation of diffusion measurements.

The following differential equations describe the boundary conditions. On the left side, no hydrogen is injected, but hydrogen which is transported into the chamber by diffusion flows out:

$$\frac{pV_l}{RT}\frac{\partial c_l}{\partial t} = -qc_l + \frac{p}{RT}DA\nabla c_1$$

where V_l is the volume of the left chamber in m³, q is the injection rate in mol/s, A is the end face of the rock sample, $\nabla c_1$is the space derivative of the hydrogen concentration at position 1, c_l is the hydrogen concentration in the left chamber. On the right side, a similar differential equation is solved:

$$\frac{pV_r}{RT}\frac{\partial c_r}{\partial t} = -\frac{p}{RT}DA\nabla c_2$$

where V_r is the volume of the right chamber in m³, ∇c_2 is the spatial derivative of the hydrogen concentration at position 2 and c_r the hydrogen concentration in the right chamber.

As an example, Figure 7 shows a comparison of a measurement with the simulation model. This measurement was done at 125 bar and 40 °C. The determined effective diffusion coefficient is $1.25 \cdot 10^{-7}$ m²/s.

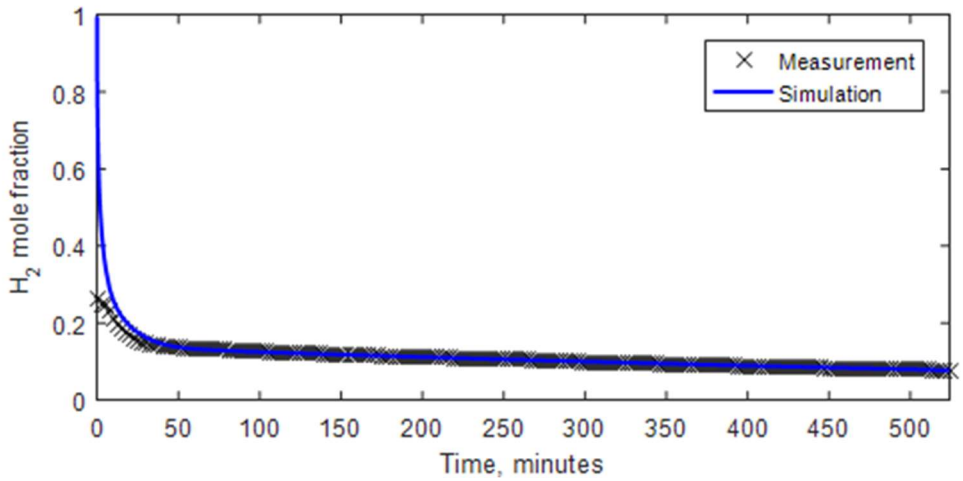

Figure 7. Comparison of the simulation results with the measurement.

3.4 Results and discussion

As reference conditions for the diffusion measurements a pressure of 100 bar and a temperature of 40 °C was chosen. All samples were measured at these conditions. In addition, every sample was measured at the respective site conditions. The Bentheimer sandstone sample was used to investigate the influence of pressure, temperature and water saturation on diffusion. Altogether, 29 diffusion measurements were performed covering a pressure range of 50 to 287.5 bar and a temperature range of 25 to 100 °C. All measurement results are presented in the data set of deliverable D4.3 “Data for: HyUSPRe - Work Package 4 - Hydrogen reservoir flow behaviour: Measurements of molecular diffusion, mechanical dispersion and relative permeability” (Michelsen et al. (2023)).

Figure 8 to Figure 10 show the behaviour of the effective diffusion coefficient in dependence of pressure, temperature and water saturation for the Bentheimer sandstone sample.

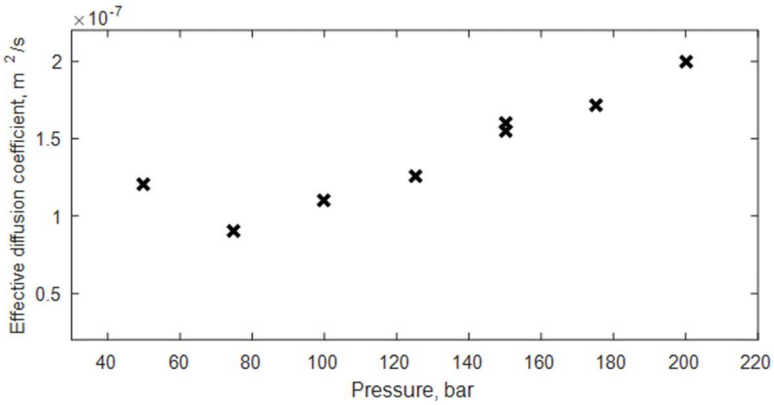

Figure 8. Effective diffusion coefficient vs. pressure for the Bentheimer sandstone sample at 40 °C.

As in the plot depicted, the effective diffusion coefficient decreases with increasing pressure, in the lower pressure range. The smallest effective diffusion coefficient occurs at a pressure

of 75 bar. At pressures above 75 bar the effective diffusion coefficient increases with higher pressure.

The following equation (Helmig, 1997) for the effective diffusion coefficient D_{pm} is a combination of the formula by (Vargaftik, 1975) for the description of the Fickian diffusion coefficient of binary gases and the model by (Millington and Quirk, 1961):

$$D_{pm} = \phi^{4/3} S_g^{10/3} D^0 \frac{p_0}{p_g} \left(\frac{T}{T_0}\right)$$

Based on this equation it can be assumed that the effective diffusion coefficient is inversely proportional to pressure, a behaviour as it appears between the two data points at 50 and 75 bar. However, the measurements show a different trend for higher pressures. From 75 to 200 bar there is a clear rising trend. A similar dependence of the diffusion coefficient on pressure was observed by Guevara-Carrion et al. (2019) for the binary system of CH_4 and CO_2.

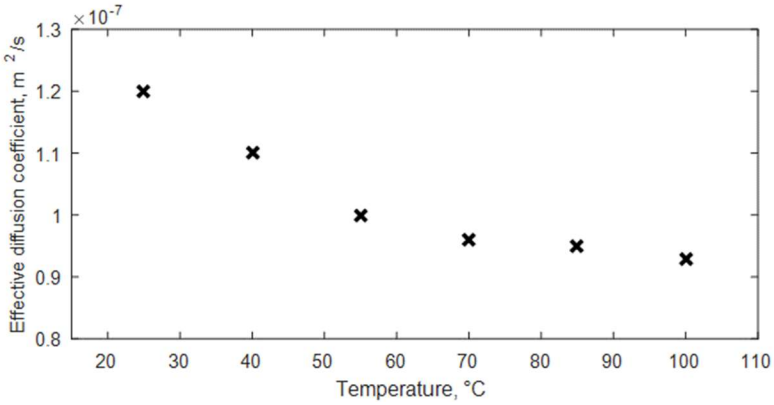

Figure 9. Effective diffusion coefficient vs. temperature for the Bentheimer sandstone sample at 100 bar.

The effective diffusion coefficient shows a decreasing trend with increasing temperature. This trend is the opposite than expected but it was also observed by Guevara-Carrion et al. (2019) along certain pathways in the supercritical region.

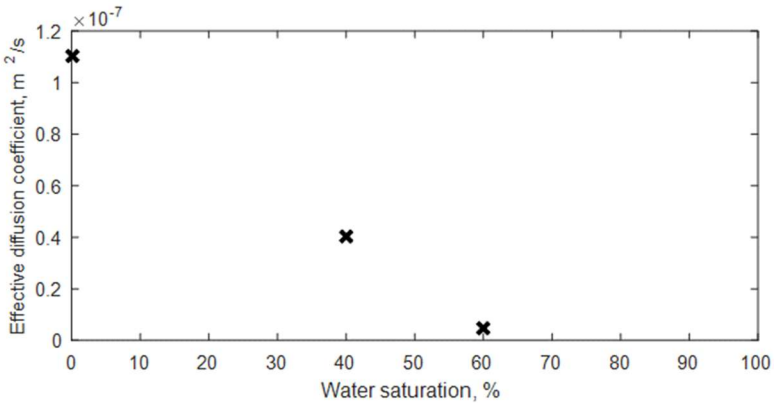

Figure 10. Effective diffusion coefficient vs. water saturation for the Bentheimer sandstone sample at 100 bar and 40 °C.

As water saturation increases, there is clear decrease in the effective diffusion coefficient, with the dry core sample having the highest effective diffusion coefficient of $1.10 \cdot 10^{-7}$ m^2/s, the sample with 40 % water saturation having $4.00 \cdot 10^{-8}$ m^2/s, and the 60 % water saturation sample having $5.00 \cdot 10^{-9}$ m^2/s. This aligns with the expectation that an increased water saturation reduces the pore space available for gas diffusion in the rock sample, and is consistent with the Millington and Quirk correlation.

4 Measurement of mechanical dispersivities

4.1 Experimental setup and procedure

The experiments for the investigation of mechanical dispersivity were carried out at the Clausthal University of Technology. The experimental setup consists of a slim tube coil with a length of 25 m which is filled with glass beads representing the porous medium (porosity approx. 35 % and permeability approx. 50 D). For determining the porosity of glass bead filling glass beads of the same kind were filled into a container and then measured by using a gas pycnometer. The permeability was determined by measuring the differential pressure between the inlet and the outlet of the slim tube coil during nitrogen injection at a constant rate.

As a preparation step for the measurements, the setup and mainly the slim tube coil is filled with methane. Then during the measurement, hydrogen is constantly injected into the slim tube. It flows through the slim tube and displaces the methane. Behind the slim tube coil is a backpressure regulator, which keeps the pressure constant. The composition of the outflowing gas mixture from the slim tube is analyzed by a gas chromatograph. A sketch of the experimental setup is shown in Figure 11.

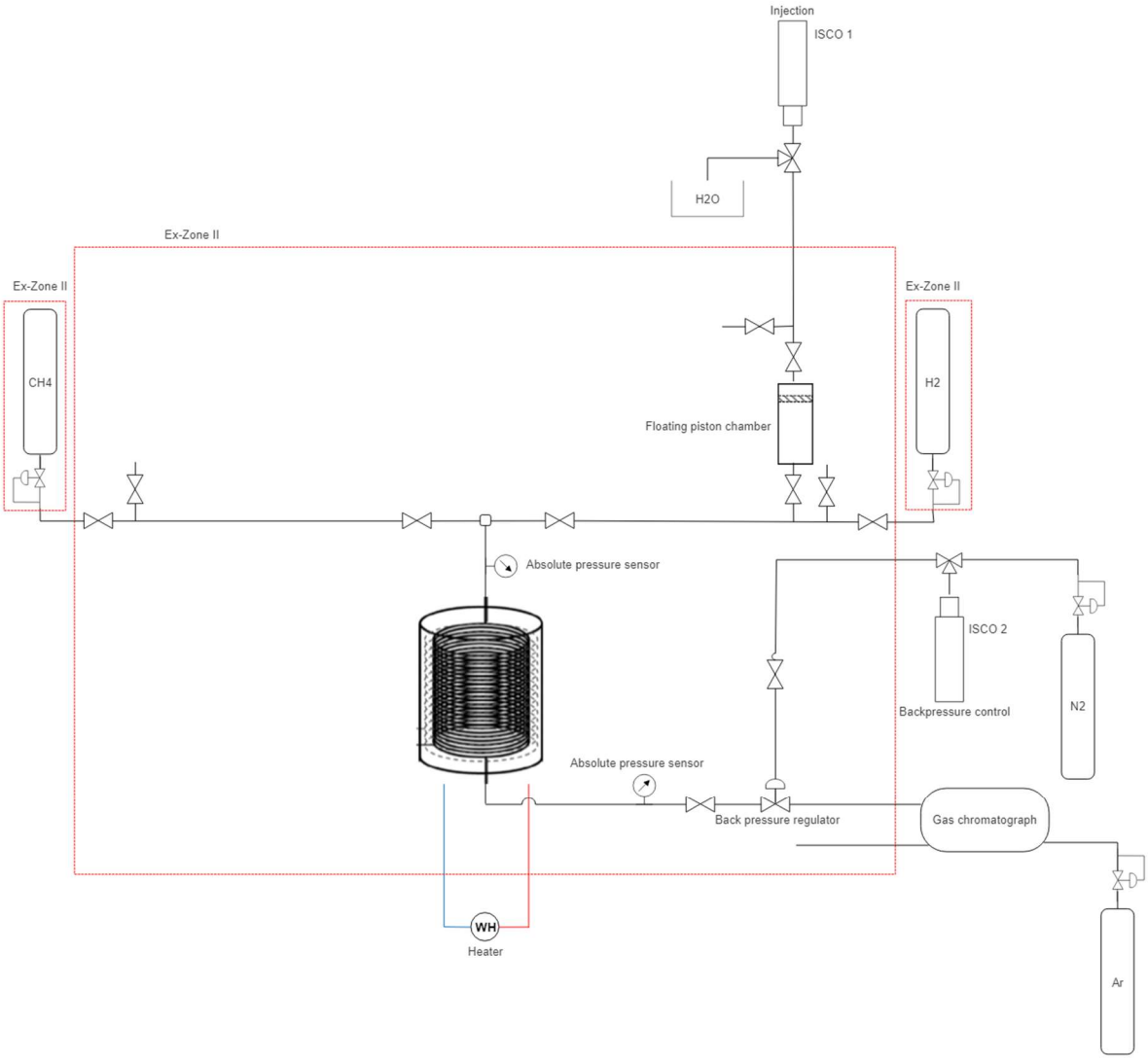

Figure 11. Sketch of the experimental setup for dispersion measurements.

4.2 Interpretation and calculation of mechanical dispersivity

The measurements were analyzed by using Scheidegger's theory for mechanical dispersion. In Scheidegger's law the dispersion tensor is linear-proportional to the true (average) flow velocity which is larger in the longitudinal (parallel to the main flow direction) direction than in the transverse (perpendicular to the main flow direction) direction (Scheidegger, 1961). As the cross-sectional area of the slim tube is very small, the measurements allow only determining the longitudinal dispersivity.

As an example, the H_2 mole fraction of the outflowing gas versus time is shown in Figure 12 for a measurement with a flow velocity of 15 m/day, a pressure of 100 bar and a temperature of 40 °C. It can be seen that the H_2 mole fraction is 0 for the first 35 hours. Then, it starts to increase and stabilizes after some hours again at a mole fraction of 1.

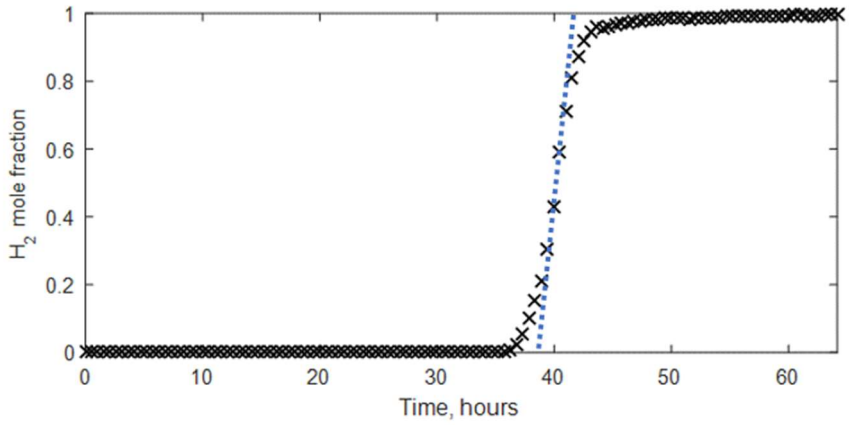

Figure 12. H_2 mole fraction of the outflowing gas vs. time (15 m/day, 100 bar, 40 °C).

This measurement data allows the determination of the longitudinal dispersity by using the following relation which was derived by neglecting the influence of molecular diffusion (Bear, 2013):

$$\alpha_L = \frac{U^2}{4\pi i^2}$$

where α_L is the longitudinal dispersivity in m, U is the true flow velocity in m/s and i is the slope of the curve in Figure 12 at a H_2 mole fraction of 0.5 in 1/s. As an alternative, the dispersivity can be determined by performing a model fitting process using a one-dimensional numerical simulation model. Further detail of the model can be found in the HyUSPRe project report D6.1 "Integrated modeling approach for the overall performance, integrity, and durability assessment of hydrogen storage at the reservoir and near-wellbore scale" by Hogeweg et al. (2023).

Figure 13 shows the comparison of the simulation with a laboratory measurement. The measurement was done at 100 bar, 40 °C and a flow velocity of 15 m/day.

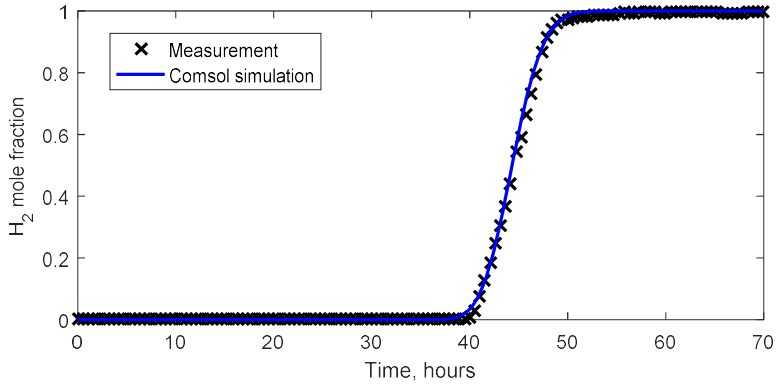

Figure 13. Comparison of the simulation results with the measurement.

4.3 Results and discussion

In total 13 dispersion measurements were carried out. Measurements were performed at temperatures from 20 to 100 °C, pressures from 50 to 150 bar and flow velocities from 5 to 50 m/day.

Since a flow velocity of 50 m/day might cause a flow regime which is in the transition from laminar to turbulent flow, the Reynolds number, Re, was calculated by using the following equation to confirm that the flow is still in the laminar regime (Bear, 2018):

$$Re = \frac{V\sqrt{k/\phi T^*}}{v}$$

Here, V is the flow velocity in m/s, k is the permeability in m² and ϕ is the porosity. T^* is the tortuosity and v is the kinematic viscosity in m^2/s. Assuming a flow velocity of 50 m/day, a permeability of 50 D, a porosity of 35 %, a tortuosity of 2 and a kinematic viscosity of hydrogen of $1.34 \cdot 10^{-6}$ m^2/s, the Reynolds number is 0.036. This value clearly indicates that the flow regime is still laminar and not turbulent.

The results are summarized in the data set of deliverable D4.3 (Michelsen et al. (2023)). All measurements were carried out in dry condition. It must be mentioned that pore storages usually contain water and that the dispersivity in a two-phase saturated system could be larger.

In Figure 14 to Figure 16 the calculated dispersivities are plotted versus true flow velocity, pressure and temperature, respectively.

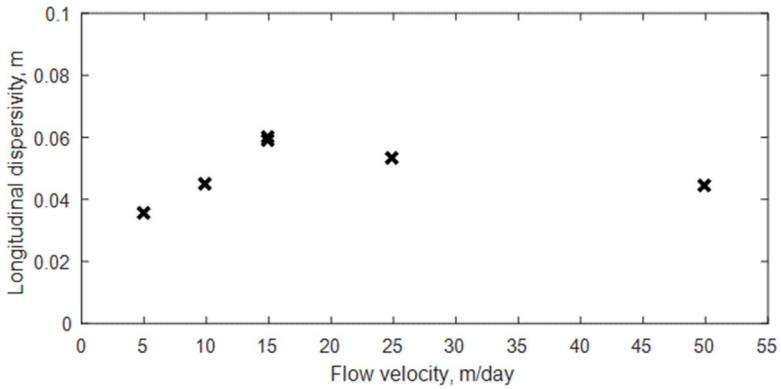

Figure 14. Dispersivity vs. flow velocity

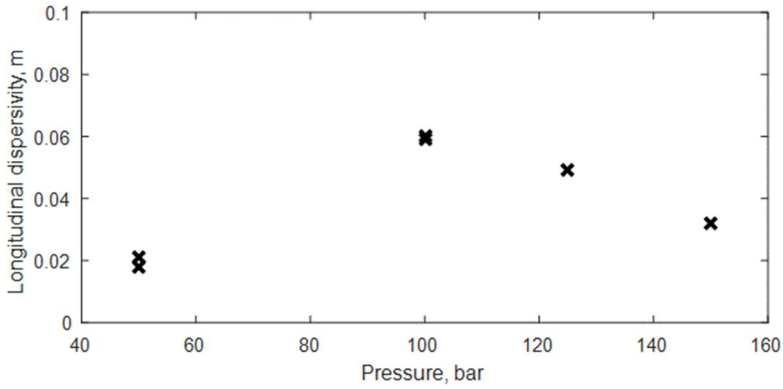

Figure 15. Dispersivity vs. pressure (flow velocity 15 m/day)

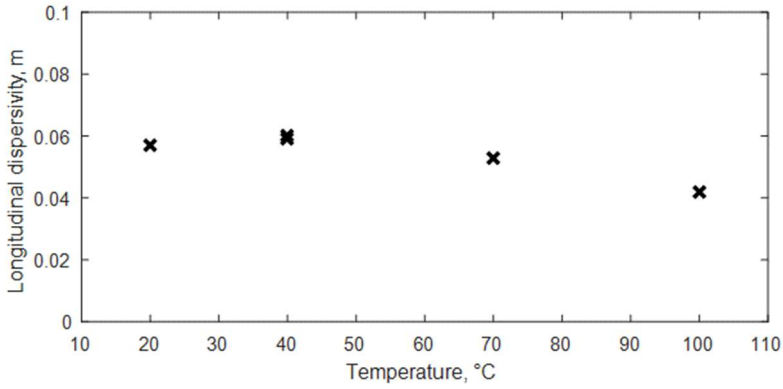

Figure 16. Dispersivity vs. temperature (flow velocity 15 m/day).

In Figure 14 to Figure 16 it can be seen that the interpreted dispersivity under different pressures, temperature and flow velocities varies by a factor of up to three. The influence of temperature is minor as the determined dispersivities are between 0.042 and 0.060 m. The influences of pressure and flow velocity are more pronounced. Both plots show a peak for the measurement at 100 bar and 15 m/day. To make sure that this peak is not a measurement mistake it was repeated leading almost exactly to the same result. As the dispersivity is a porous medium (or rock) property, it should theoretically not be dependent on pressure, temperature or flow velocity. The results of this study show that Scheidegger's theory for dispersion allows to predict dispersive mixing between two gases under subsurface storage

conditions sufficiently good, however, it can be recognized that there are some effects which are not captured by this law. Relatively high deviations at different pressures (cf. Figure 15) were observed which could be an implication of pressure-dependent fluid properties like density and/or viscosity. The plot of dispersivity versus flow velocity (cf. Figure 14) shows that the relationship between the dispersion tensor and the flow velocity is not ideally linear, however, taking an average value would allow to obtain a close match under all conditions.

In the literature there is one study which allows a comparison to our measurements. Kurihara et al. (2000) also did a displacement experiment in a slim tube coil. They used argon to displace methane in a slim tube with a length of 12 m. The determined longitudinal dispersivity was ca. 0.012 m, similar to our results.

5 Hydrogen relative permeability experiments

5.1 Methodology

5.1.1 Rock samples

Two sandstone and one carbonate rock samples were used for the displacement tests. Samples from HyUSPRe industry partners were not available at the time of writing, so analogous were used. The mineralogy and pore structures of the rock samples were characterized using XRD analysis, MICP experiments, and centrifuge capillary pressure test (see Figure 17, Table 4). The full details of these experiments are provided in the Supporting Information (SI). The porosities of the samples were measured using the buoyancy technique based on Archimedes principle (Melnyk & Skeet, 1986).

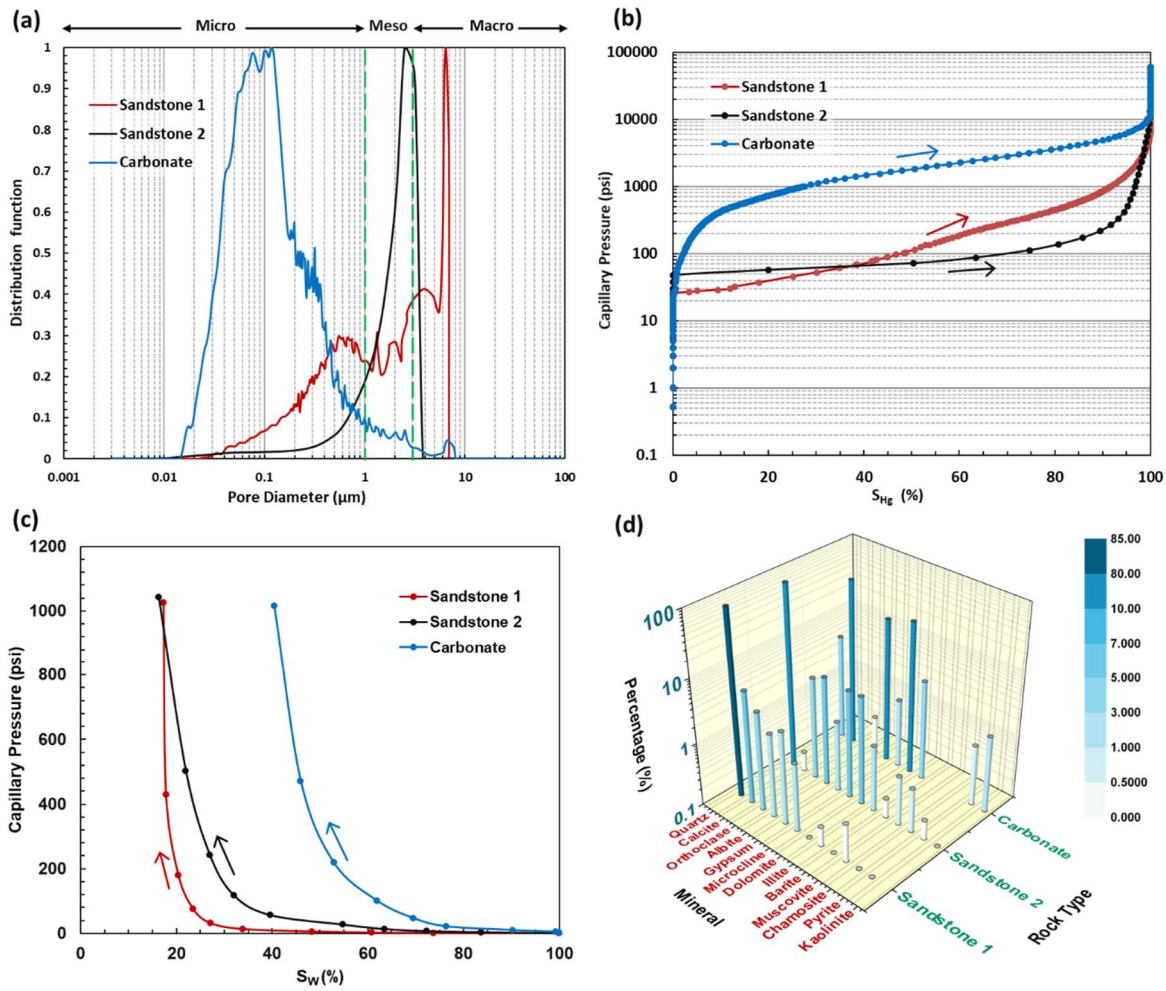

Figure 17. Analysis of different properties of the rocks used in this study: (a) Pore size distribution as determined by MICP method (b) Capillary entry pressure versus mercury saturation as determined by MICP method (c) Capillary entry pressure for air versus water saturation as determined by centrifuge capillary pressure test (d) Bulk mineral composition of each sample as determined by XRD analysis (see Table S1) (Rezaei et al., 2022).

Table 4. Physical properties of the cores used within this study.

Rock Type	Length [cm]	Diameter [cm]	Porosity [%]	Liquid Permeability [mD]
Sandstone 1 (S1)	9.46	3.81	16.44	34.36
Sandstone 2 (S2)	8.97	3.81	10.52	11.18
Carbonate (C1)	8.88	3.81	12.82	3.31

5.1.2 Core-flooding experiments

After vacuum drying at 70 ℃, the core samples were loaded into a Hassler type core holder (Figure 18) and saturated with sodium chloride brine (NaCl, certified purity of 99.5 %) of a certain salinity. Subsequently, the brine was injected at three different flow rates to determine the brine permeability, K_w, using the Darcy equation. The obtained K_w was used as the base fluid (absolute) permeability for the relative permeability calculations. The desired gas (i.e., H_2, CH_4, or N_2; all research-grade with a purity of 99.9995 vol%) was injected into the brine-saturated core sample with a pre-defined constant pressure (see Table 5) determined by the core's K_w value. The inlet and outlet gas flow rates, the differential pressure between the core faces (i.e., inlet and outlet), and the produced effluent brine volume were recorded with time during the injection process and recording continued until no more brine was seen in the effluent (i.e. when water cut/ratio of water to total fluids is approximately zero).
Temperature was controlled via a fan oven housing in the core holder (Figure 18). A pressure gauge, Rosemont 3051 pressure transmitter from Emerson, Netherlands, was used to continuously record the differential pressure across the sample (i.e. between inlet and outlet face of core sample) value during flooding experiments.

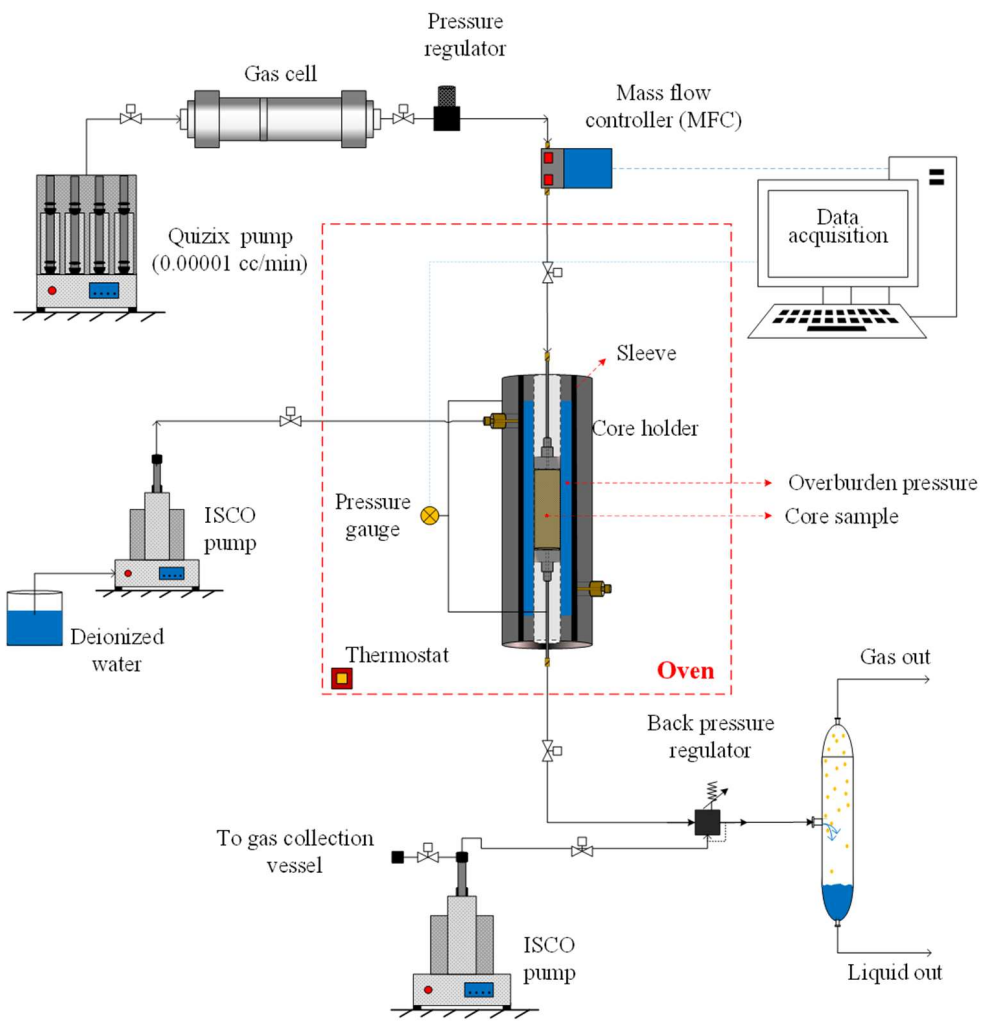

Figure 18. Schematic of the setup used for gas-brine relative permeability measurements; to restrain gravity segregation into the core sample during the gas injection process, the core holder is placed in a vertical mode. The sizes of different objects have been re-scaled to make them visible (Rezaei et al., 2022).

5.1.3 Relative permeability calculations and simulations

The recorded data was used to calculate the relative permeabilities of gas (K_{rg}) and brine (K_{rw}) as a function of gas saturation using the Johnson, Bossler, and Naumann (JBN) method (Johnson et al., 1959). They developed an analytical technique for calculating relative permeabilities based on unsteady state fluid displacement data obtained from constant pressure experiments. In this method, the relative permeability for gas can be determined using the following equations:

$$K_{rg} = \frac{\Delta G_{inj}}{\Delta t} C_2 \quad (1)$$

$$C_2 = \frac{\mu_g L C_1}{A K_1 \Delta P} \quad (2)$$

$$C_1 = \frac{P_a}{P_m} \quad (3)$$

where:

K_{rg}	Relative permeability of the gas phase
Δt	Time interval
μ_g	Dynamic viscosity of the gas phase
ΔP	Differential pressure between inlet and outlet
ΔG_{inj}	injected gas volume at the time interval
L	Core plug length
A	Cross sectional area of the plug
K_1	Absolute brine permeability
C_1	Boyle's constant
P_a	Atmospheric pressure
P_m	mean pressure

Considering f_{w2} (Eq. 4) as water fractional flow, the relative permeability of brine can be calculated using Eq. 5:

$$f_{w2} = \frac{q_w}{q_w + q_g} \quad (4)$$

$$f_{w2} = \frac{1}{1 + \frac{K_{rg}}{K_{rw}} \frac{\mu_w}{\mu_g}} \quad (5)$$

where q_w and q_g are the instantaneous oil and gas flow rates, respectively.

History matching was used to simulative the relative permeability from experimental data. The Modified Corey model for relative permeability was used to determine the parameters of the models using the software CYDAR®.
Experimental and theoretical evidence have established that relative permeabilities are influenced by many rock and fluid parameters. Accordingly, an extended series of drainage relative permeability, residual gas saturation, and drainage capillary pressure tests in sandstone and carbonate core samples at various salinity and pressure conditions were undertaken to investigate the flow behaviour of hydrogen gas relative to the formation brine in porous media. In addition, core flooding experiments were performed using N_2 and CH_4 to compare the flow behaviour of different gases at high pressure conditions. Table 5 lists all tested core-flooding scenarios.

5.2 Results and Discussion

We experimentally determined hydrogen/brine relative permeability for a range of conditions (Table 5) and different geological settings with a particular focus on comparing it to natural gas relative permeability curves. Unsteady state drainage relative permeability curves and best fits with the modified Corey models (see SI Table S2 for the fitted parameters) for different experiments are shown as a function of gas saturation in Figure 19. In all nine experiments, drainage relative permeability is characteristic of a strongly water-wet system as the wetting phase (brine) relative permeability decreased rapidly at relatively low gas saturations due to its occupancy of smaller and less permeable pores, and curves vary as expected with gas type, salinity, pressure and bulk rock characteristics. It must be noted that this is an early study and the impact of any additional influencing parameters, such as the presence of impurities in the gas phase or specific minerals in rocks, must be explored further in future studies.

Table 5. Different core flooding experiments.

Exp. No.	Rock sample	Gas type	Back Pressure [MPa]	Salinity [ppt]	Temperature [K]
1	Sandstone 1	H_2	0.1	35	353.15
2	Sandstone 1	H_2	10.34	35	353.15
3	Sandstone 1	H_2	20.68	35	353.15
4	Sandstone 1	H_2	20.68	100	353.15
5	Sandstone 1	H_2	20.68	200	353.15
6	Carbonate 1	H_2	20.68	35	353.15
7	Sandstone 2	H_2	20.68	35	353.15
8	Sandstone 2	N_2	20.68	35	353.15
9	Sandstone 2	CH_4	20.68	35	353.15

5.2.1 Effect of pressure

Unsteady state drainage relative permeability experiments were conducted to determine the relative permeability-saturation relationship for the H_2/brine system in core S1 at three different backpressure values (0.1, 10.34, and 20.68 MPa). Figure 20a shows that the effect of pressure on the relative permeability of H_2 against brine is similar to any other typical gas at higher pressure; this is driven by the effect of pressure on the viscosity and IFT of the hydrogen gas. An increase in pressure results in higher H_2 viscosity, which subsequently leads to a reduction in gas mobility and the relative permeability of hydrogen. As a result, the rate of hydrogen injection and recovery at greater depths will be slightly lower than that at higher depths. It should be noted that at lower gas saturations, higher pressures showed higher hydrogen relative permeability (Figure 20a). This shows that at lower gas saturations capillary forces overcome viscous forces and as such lower IFT at higher pressures causes an increase in the relative permeability of hydrogen with pressure. When comparing the relative permeability of H_2 at various pressures, it is evident that H_2 has a much higher relative permeability at ambient conditions than at higher pressures. However, at higher pressures, the relative permeability of H_2 is almost constant. Since wetting state determines the relative permeability at endpoints (Yoshida et al., 2016), these results show that pressure has a significant impact on wettability at lower pressures and almost no impact at higher pressures.

5.2.2 Effect of salinity

At a constant backpressure of 20.68 MPa, core S1 was selected for H_2-brine relative permeability measurements at three different NaCl salinities (35 ppt, 100 ppt, and 200 ppt). As shown in Figure 20b, the increase in NaCl concentration has little impact on the relative permeability curves. The higher salinity experiments showed slightly lower relative permeabilities for hydrogen, which implies that H_2 will move less easily through higher salinity pore fluid systems. Like other gases, salinity increases the H_2/brine IFT which increases the required capillary pressures for drainage and slightly reduces the relative permeability of the non-wetting phase (i.e. H_2). Similar behaviour has been observed for CO_2 gas in other studies (Bachu & Bennion, 2008; Jamaloei, 2015; Middleton et al., 2012). Furthermore, the increase in NaCl concentration is expected to reduce the hydrogen solubility (salting-out effect) in a manner proportional to the salt concentration until full saturation of the solution is reached. In addition, the affinity of H_2 molecules to the solid surfaces of the rock minerals would increase

(slightly affecting the wettability), which makes it more difficult for hydrogen to move through the porous medium.

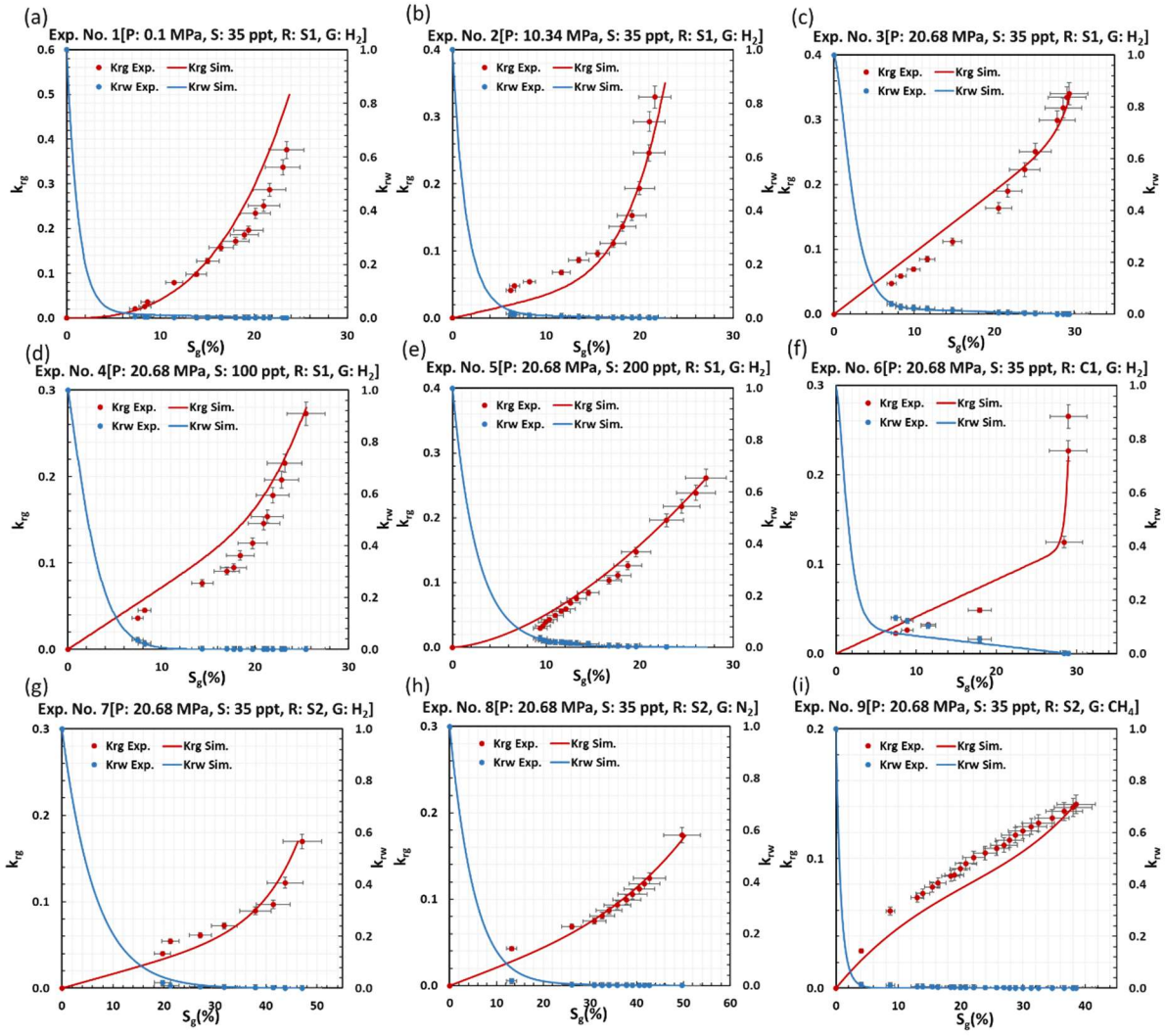

Figure 19. (a-g) Drainage H_2 and different brine relative permeability curves for 2 sandstone and 1 carbonate samples at different pressures. (h) Drainage N2 and brine relative permeability curves for sample S2. (i) Drainage CH_4 and brine relative permeability curves for sample S2 (Rezaei et al., 2022).

5.2.3 Effect of rock type

To investigate the flow behaviour of H_2 gas and brine (3.5 wt.%) in different types of rocks (i.e varying pore structure and mineralogy), the relative permeability of H_2-brine was measured for a carbonate rock and 2 different types of sandstones at 20.68 MPa backpressure. A comparison of these rocks (Figure 20c) shows a strong relationship between rock structure and relative permeability. Sandstone 1, with the highest absolute permeability (34.36 mD), has the highest relative permeability and it also has the highest porosity of the tested samples (16.44 %; Table 4). The carbonate rock had the second highest relative permeability, despite having the lowest absolute permeability (3.31 mD) and the lowest mean pore diameter of the samples tested, it had the second highest porosity of 12.82 %. Sandstone 2 had the lowest relative permeability and also had the lowest porosity (11.18 %). Taken together, these results

suggest that the relative permeability of hydrogen increases with porosity and is less dependent on pore size. We could not find a direct relationship between pore size distribution and mineralogy with hydrogen relative permeability within this study.

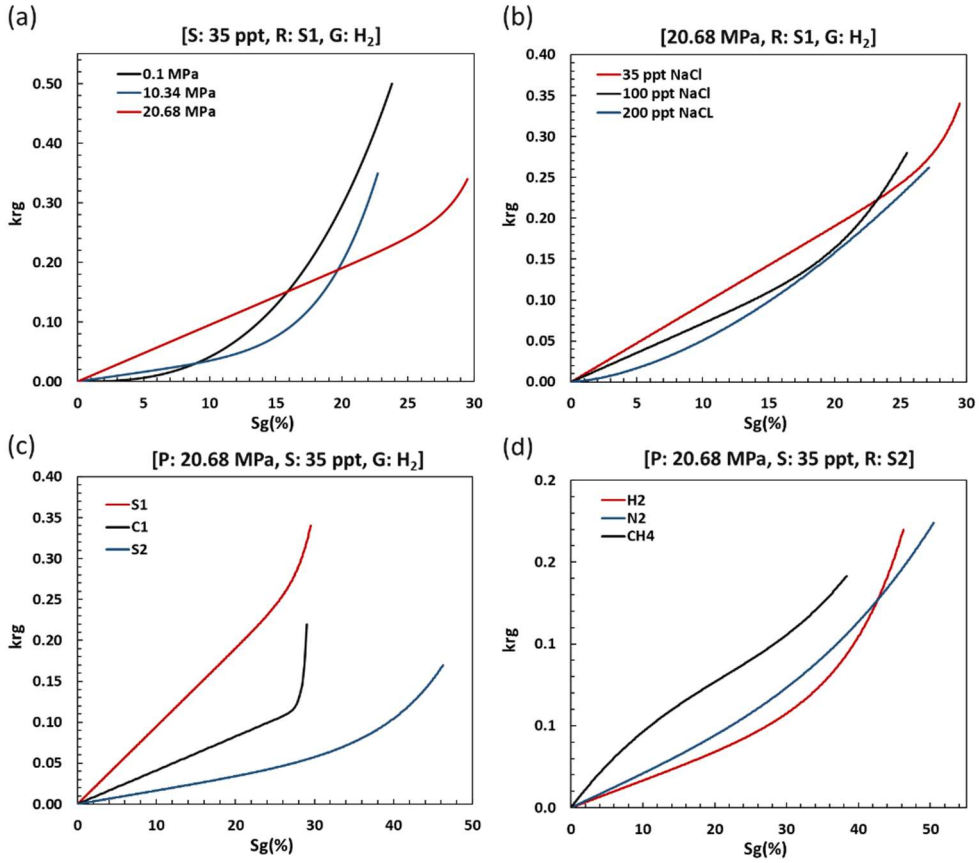

Figure 20. Drainage gas relative permeability curves versus gas saturation to compare (a) effect of pressure on drainage hydrogen relative permeability (b) effect of salinity on hydrogen drainage relative permeability (c) effect of rock type and rock pore structure on hydrogen drainage relative permeability (d) hydrogen drainage relative permeability with that of N_2 and CH_4 (Rezaei et al., 2022).

5.2.4 Comparison to other gases

Core sample S2 was used for drainage relative permeability tests of the N_2-brine, CH_4-brine, and H_2-brine systems. All measurements were performed at the same backpressure (20.68 MPa), and brine salinity (35 ppt). As can been seen in Figure 20d, CH_4 exhibited a higher relative permeability at a given brine saturation, whereas H_2 and N_2 had higher maximum relative permeability because of higher endpoint gas saturations. This may also be justified by the fact that hydrogen has a higher IFT than CH_4, which either causes H_2 to invade fewer, larger pores or that the effect of interfacial forces are higher than viscous forces at higher water saturations. However, when the gas saturation reaches the maximum, H_2 has a higher relative permeability than CH_4, which is directly related to the lower viscosity of H_2. It should be noted that further investigation is required to understand the specific reasons behind these observations. This behaviour overall is favourable for geological hydrogen storage as at higher water saturations, hydrogen will have a lower relative permeability which reduces the risk of viscous flow and increases the sweep efficiency. In addition, the higher relative permeability of H_2 at high gas saturations will help achieve better recovery rates of hydrogen. Comparing H_2/brine and CH_4/brine drainage relative permeability curves reveal that H_2 will have more

favourable flow behaviour than methane during both storage and recovery stages. The comparison of the H_2/brine and N_2/brine systems shows that H_2 and N_2 have very similar relative permeability curves, suggesting N_2 may be used as a substitute for hydrogen in flow experiments, resulting in a reduced risk for health and safety.

5.2.5 Comparison to other studies

This unsteady state study on the drainage relative permeability showed that from an injectivity and recovery perspective, shallower, i.e. lower pressure sites, are recommended for future H_2 storage operations in porous media due to a reduced relative permeability at higher H_2 saturations and high pressures of 10.68-20.68 MPa, albeit similar maximum gas saturations at 0.1 MPa and 10.34 MPa (Figure 20a). This is in contrast to previous findings by Yekta et al. (2018) who documented little change of the H_2 relative permeability during drainage at pressure increases of from 5.5 MPa to 10 MPa using the steady state method. In addition, this study showed good similarity between H_2 and N_2 between the drainage relative permeability curves (Figure 20d), in contrast to previous reports of divergent displacement behaviour of H_2 and N_2 using the steady state method (Lysyy et al., 2022b).

While it is known that unsteady state and steady state relative permeability measurements yield different magnitudes of relative permeability (Ibrahim and Koederitz, 2001), general trends in the data under different conditions can be expected to be the same. A very important determinant for the outcome of any fluid flow study are the type of forces acting under a given experimental condition. When gravitational and capillary forces dominate, there a clear temperature and pressure dependency on the fluid flow, injectivity, and recovery can be expected, and different gases will show different displacement patterns. When buoyancy and capillary forces dominate, there is no temperature and pressure dependency on the flow of a gas and gases should behave similarly at any set experimental condition.
In the drainage relative permeability experiments of this study the core was placed vertically, and H_2 was injected into a brine-saturated core (unsteady state). Under these conditions, buoyancy and capillary forces should dominate, so no difference between the relative permeability of H_2 and N_2 was expected. In the study by Lysyy et al. (2022) the core was also placed vertically but H_2 and brine were flowing at the same time (steady state) so gravitational forces acted on the displacement, explaining the difference in the observed relative permeabilities of H_2 and N_2.

A pressure effect was not anticipated under the experimental conditions of this study. In addition, it was somewhat surprising that CH_4 showed a higher permeability than H_2 and N_2. Boon and Hayibeygi (2022) recently highlighted the importance of visualising H_2 flow through rock during relative permeability experiments, as low permeability regions in a rock may cause channel flow of one fluid, causing deviations to the predicted flow behaviour and impeding a determination of the relative permeability.

6 Hydrogen injectivity and recovery experiments

6.1 Methodology

6.1.1 Core-flooding experiments

We performed unsteady and steady state, two-phase core flooding experiments with H_2 (purity 99.9995 vol.%, BOC Ltd.) and brine (0.5 M CsCl or 2 M KI, Sigma-Aldrich) in a Clashash sandstone (Permian, aeolian sandstone from near Elgin in Scotland. The composition of Clashach is: ~96 wt.% quartz, 2 % K-feldspar, 1 % calcite, 1 % ankerite (Iglauer et al., 2012), porosity 11.1-14.4 % (Iglauer et al., 2012; Iglauer et al., 2013; Pentland et al., 2010)) at ambient temperature (~293 K). The Clashach sandstone, with its low mineralogical variability, yet still comparably big pore space, was chosen in order to facilitate the visualization of the injected H_2 and the interpretation of the results.
Experiments were carried out at the University of Edinburgh using the in-house micro-CT instrument and were aimed at imaging the displacement and capillary trapping of H_2 by brine as a function of saturation after drainage and imbibition under different experimental conditions. Three experiments were carried out that investigated the effect of injection pressure (2-7 MPa), whereof each was repeated once (Exp. 1-3, Table 6). The standard error on the H_2 saturation in the repeated experiments was calculated as the standard deviation divided by the square root of the number of repeated experiments. Experiment 4 used N_2 instead of H_2. This experiment was undertaken in order to compare the flow behaviour of the two gases, which is of relevance because N_2 is sometimes used as an analogue for H_2, e.g. in permeability measurements (Rezaei et al., 2022; Flesch et al., 2018). Because rearrangement processes in the pore volume were noted previously for N_2 (Cao et al., 2019), exp. 5 (Table 6) was undertaken to examine the stability of H_2 in the rock volume over an experimental duration (10 hours): Ten PV of H_2 were injected into a brine-saturated rock and keeping the pressure constant inside the pressure vessel, with imaging undertaken at the start and after 10 hours.
The experiments used a bespoke x-ray transparent core holder for a 5 mm diameter rock core, which was a scaled-up version of the cell described by (Fusseis et al., 2014). The specifications of the pressure vessel of PEEK were engineered with safety factors of 2 times the maximum applied confining pressure (9 MPa; Table 6).
Rock cores for the experiments were obtained by diamond drill coring with a water-flushed chuck, followed by preparation of the core ends by grinding on a lathe. Experiments used a set of four high-pressure pumps (Cetoni Nemesys™, flowrate range 0.072 nl s^{-1} to 13.76 ml s^{-1}): One for the injection of H_2, one for the injection of brine, one to hold the backpressure and one for the confining pressure (Figure 21). A bespoke manifold system composed of high-pressure 1/8" and 1/16" 316 stainless steel and 1/16" PEEK tubing (Swagelok, Top Industrie and Cole Parmer, respectively) connected the pumps to the core-flood cell (Figure 21). Additional pressure transducers (ESI Technology; accuracy 0.1 % full-scale) were coupled to the flow system at the inlet and outlet to allow for higher precision pressure monitoring than was possible using the integral pressure gauges in the syringe pumps.
Cyclic H_2 and brine injections used a Clashach outcrop sample without further cleaning of 4.7 mm diameter and a relatively long length of 54-57 mm to avoid the influences of capillary end effects (Pak, 2014; Kumar et al., 2009). To prevent leakage of H_2 into the confining fluid, the rocks were jacketed in aluminium foil and polyolefin heatshrink tubing and sealed with silicone adhesive between the conical-ended pistons within the pressure vessel. All experiments were commenced by saturating a water-wet rock with brine (0.5 M CsCl) at a flow rate of 70 µl min^{-1}. Afterwards, H_2 was injected (drainage) into the brine-saturated rock at flow rates of 20-80 µl min^{-1}, based on a desired capillary-regime capillary number, N_C, of 1.7-6.8x10^{-8} (The viscosity

of H_2 is 9.01 µPa s at 298K and 4.7 MPa (Yusibani et al., 2011) and the IFT between H_2 and water is 72.6 mN m^{-1} at 298K and 5 MPa (Chow et al., 2018; Chow et al., 2020)). Subsequently, the brine was reinjected (imbibition) at flow rates of 20-80 µl min^{-1}, resulting in N_C of 2.35-9.45x10^{-6} (using the same IFT between H_2 and water of 72.6 mN m^{-1} at 5 MPa and 298 K (Chow et al., 2018; Chow et al., 2020) and a viscosity of 1.247 x10^{-3} Pa s at 5 MPa that was estimated from the reported 1.2503 x10^{-3} Pa s and 1.233x10^{-3} Pa s at 0.1 MPa and 25 MPa, respectively, and 298 K (Nakai et al., 1995). The N_C the N_2 experiment was 3.5x10^{-8} (using an IFT of 73 mN m^{-1} between N_2 and water at 298K and 10 MPa (Niu et al., 2015) and a viscosity of 1.89x10^{-5} Pa s at 5 MPa and 295K (Yusibani et al., 2011)). Each injection used ten pore volumes to ensure completely flushing of the sample cores with the injected fluid.

The combined application of an x-ray transparent core holder and µCT allowed the visualization of the fluid saturation distributions at pore scale at each injection step. The difference in the x-ray attenuation coefficient of the fluids (H_2 and 0.5 M CsCl) provided an excellent contrast between the two fluid phases and the rock on the acquired µCT images, combined with the respective radiation energy in the two different laboratories.

3D volumes were acquired from the lower central portion of the sample to avoid the impact of capillary end effects on fluid saturation (Pak, 2014; Kumar et al., 2009). Image acquisition used a µCT instrument built in-house at the University of Edinburgh, comprising a Feinfocus 10-160 kV reflection source, a Micos UPR-160-air rotary table and a Perkin-Elmer XRD 0822 1 MP amorphous silicon flat panel detector with a terbium doped gadolinium oxysulfide scintillator. Data acquisition software was developed in-house. The following settings were used for the experiments: 120 keV, 16 W, 2 seconds exposure time, 1200 projections and 2 frames per stop. The voxel size was 5.4 $µm^3$.

Table 6. Overview over experiments.

Experiment	Description	Sample	H_2/brine injection ratio[s]	Flowrate [µl min^{-1}]	Injection Pressure [MPa]	Confining Pressure [MPa]	Pore volumes injected	Repetitions of experiment
Exp. 1	Primary drainage and imbibition in unsteady state displacements of H_2 and brine	1	-	20	7	9	10	1 entire repetition, 1 repetition on drainage only
Exp. 2	Primary drainage and imbibition in unsteady state displacements of H_2 and brine	1	-	20	5	9	10	1
Exp. 3	Primary drainage and imbibition in unsteady state displacements of H_2 and brine	1	-	20	2	9	10	1
Exp.4	Unsteady state displacements of N_2 and brine	1	-	20	5	9	10	-
Exp.5	H_2 stability	1	-	80	5	9	10	-

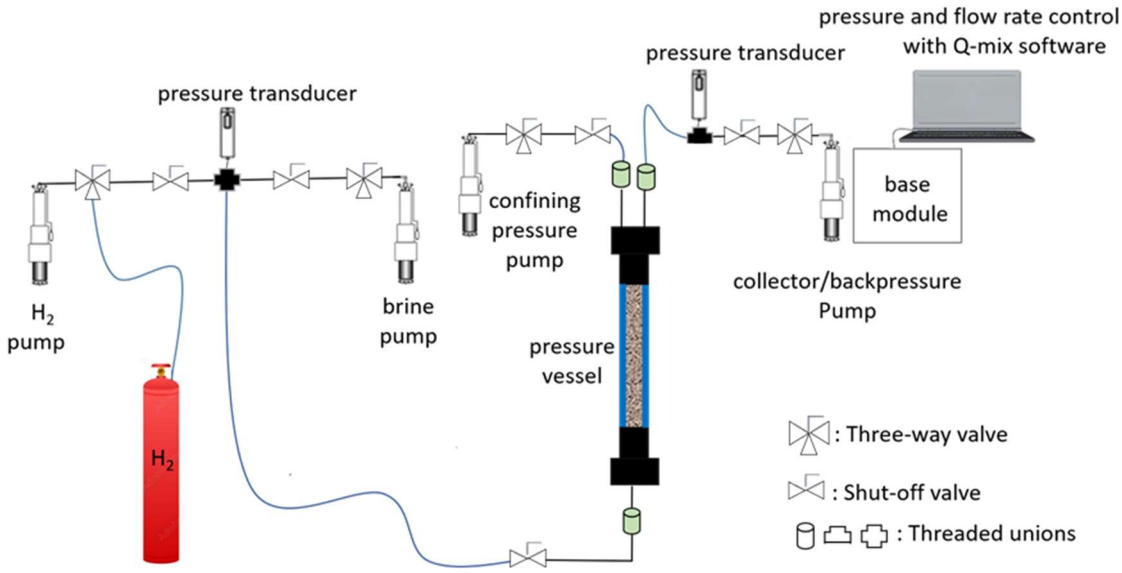

Figure 21. Experimental setup showing the manifold system that connected the X-ray transparent pressure vessel to a set of four high-pressure Cetoni NemesysTM pumps: one to inject H_2, one inject brine, one to maintain backpressure and one to maintain confining pressure. The materials for the connections were 316 stainless steel (black), HPLC (green) and PEEK or carbon fibre reinforced PEEK (blue). Pressure and flow rate control was achieved with the Q-mix software (Thaysen et al., 2022).

6.1.2 Image analysis

Tomographic reconstructions were undertaken by filtered back projection using Octopus 8.9 on a GPU accelerated workstation (Vlassenbroeck, J., et al, 2010). All subsequent image processing and analysis of tomographic data was performed using Avizo Version 9.1.1 (FEI, Oregon, USA). Experimental data were processed using a non-local means filter (Buades et al., 2005). Segmentation used a global threshold on the 2D greyscale image histogram, and encompassed two phases. In the water-saturated scans, water and rock were treated as two discrete phases. In scans after brine and H_2 injections, the H_2 was treated as one phase and the brine and rock as a single separate phase, following protocols of Andrew et al. (2014). Holes and spots which were at the resolution limit of the data were removed from all datasets (applied thresholds corresponded to 3^3 and 5^3 voxels, respectively). Based on the segmented image of the water-saturated scan in UoE experiments, a pore size distribution was calculated. The 3D image was separated into discrete pores using Avizo's 'separate objects' module, which calculates a chamfer distance map of the pore-space and then applies a marker based watershed algorithm to the distance map to define discrete pore bodies as catchment basins separated by the watershed which marks the location of pore throats.
In scans following brine and H_2 injections, the segmented image was analysed in 3D using the 'labeling' and 'label analysis' modules to identify, label and measure the volume of each H_2 cluster. Hydrogen cluster size distributions were compared to the pore size distribution to evaluate the H_2 connectivity and identify trapping mechanisms during brine imbibition.

6.2 Results

6.2.1 Hydrogen wetting behaviour and stability

Hydrogen sat in the centre of the pore bodies. Residual brine sat in corners, pore throats (Figure 22b and c) and, as a subtraction of the water saturated scan from the H_2-and brine filled rock revealed, in thin films around the grains (Figure 22d). The injected H_2 remained stable within the pore volume under no-flow conditions and at constant pore fluid pressure over a time period of 10 hours which was the maximum experimental duration (Figure 23).

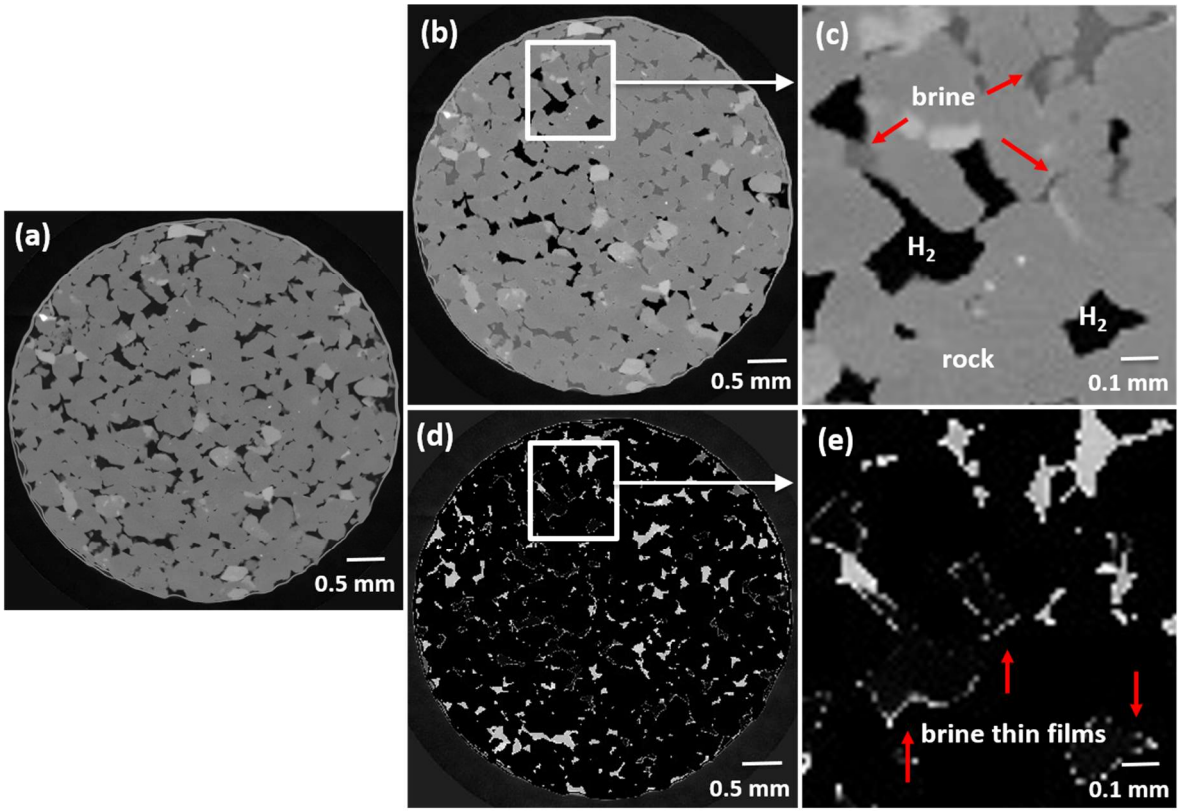

Figure 22. (a) Water-saturated Clashach sandstone with the water shown in black and the rock in different shades of grey. (b) and (c) Brine-saturated Clashash sandstone after injection of H2. H2 (black) fills the centre of the pores while the brine (dark grey) remains in corners and small pore throats around grains (different shades of grey). (d) and (e) Subtraction of the water-saturated scan from the brine-saturated scan after H_2 injection, following registration of the brine-saturated scan after H_2 injection to the water-saturated scan, revealing discontinuous brine thin films around grains. The rim around the Al foil in (d) is caused by continued shrinkage of the Al foil onto the rock during the experiments (Thaysen et al., 2022).

6.2.2 Effect of pore fluid pressure on hydrogen connectivity, saturation and recovery

Hydrogen saturation during drainage was independent of the pore fluid pressure with 49.8 %, 51.1-52.4 % and 39.7-52.9 % saturation at pore fluid pressures of 2, 5 and 7 MPa, respectively (Figure 24). Hydrogen connectivity during drainage generally showed one large, connected cluster at all pore fluid pressures except for one out of three images at 7 MPa which showed

three large disconnected clusters (Figure 24). During drainage, the largest H_2 cluster had a volume of $1x10^8$ μm^3 at all pore fluid pressures except for the one run at 7 MPa with the disconnected clusters were the largest volume was $7x10^7$ μm^3 (Figure 25e).
Hydrogen clusters during drainage were at all pore fluid pressures much larger than discrete pores with a maximum volume of $1.3x10^6$ μm^3 (Figure 25e, a). Comparing all H_2 cluster size distributions during drainage (Figure 25f) reveals that all drainage curves, including two of the distributions at 7 MPa (squares and rhombi), have largely the same distribution, however one of the three distributions at 7 MPa (triangles) is distinct. This outlier experiment corresponds to the experiment showing a lower S_{nwi} (Figure 24f).
Capillary trapping of H_2 during imbibition seemed independent of the pore fluid pressure with 10 %, 11-12 % and 4-21 % of trapped H_2 at 2, 5 and 7 MPa, respectively (Figure 24), corresponding to 20 %, 21-22 % and 11-43 % of the initially injected H_2. During imbibition, large H_2 clusters were broken down into smaller clusters (Figure 25a-d), in line with the visual changes of the H_2 clusters (Figure 24). The largest H_2 clusters after imbibition remained above the maximum pore size during all experiments except for one experiment at 7 MPa (triangles in Figure 25g, Figure 25a), showing that not only was H_2 trapped in discrete pore bodies but also as larger H_2 ganglia. The break-down of the largest H_2 clusters during imbibition caused the number of clusters in the size range log 4 to log 6 μm^3 to increase while the number of very small clusters of log 2-4 μm^3 typically decreased (Figure 25b-d). Comparing all H_2 cluster size distributions during imbibition (Figure 25g) shows that the distributions at 2 and 5 MPa are largely the same while the imbibition distributions at 7 MPa are distinct.
Injections of H_2 and brine into the same rock volume and at the same flow rates and pore fluid pressures of 2-5 MPa were repeatable with small standard errors between 0.01-0.66 % (Figure 24a-d, Figure 25b and c). At 7 MPa very distinct S_{nwi} and S_{nwr} were measured (Figure 24e-g); During drainage the standard error was 4.8 % at an average H_2 saturation of 47.4 %. The standard error during imbibition was 8.5 % at an average saturation of 12.9 %. The pressure differences between inlet and outlet during these experiments were within the error of the pressure sensors of 0.1 % full-scale.

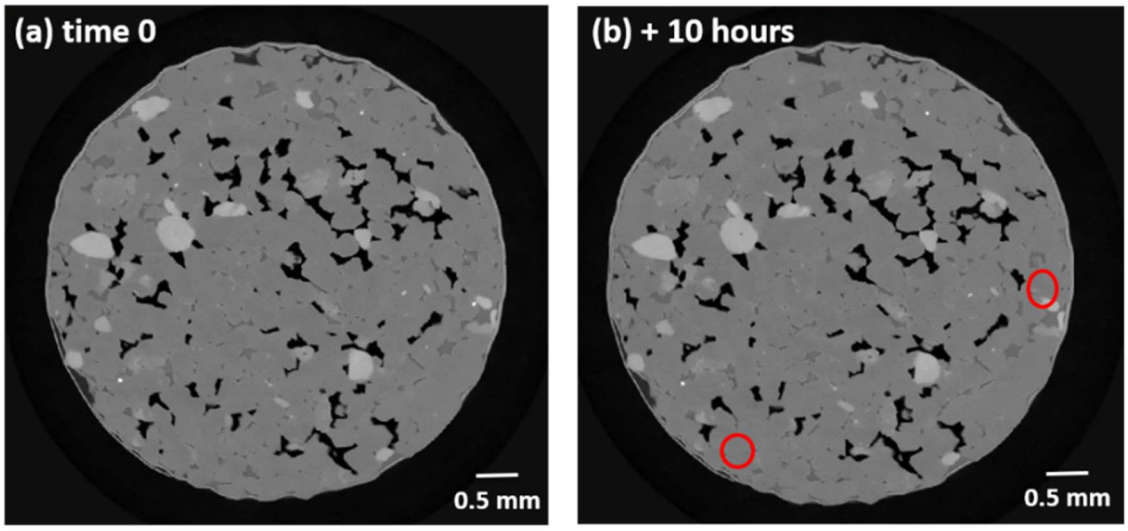

Figure 23. Hydrogen stability at 7 MPa injection pressure and a flow rate of 20 µl min-1 (capillary number $2*10^{-8}$) at time zero (a) and after ten hours (b). Red circles indicate subtle differences in the H_2 filled pore volume after ten hours. The difference in the H_2 saturation for the total scanned rock volume was within error at 49.55 % and 49.53% for time 0 and after ten hours, respectively (Thaysen et al., 2022).

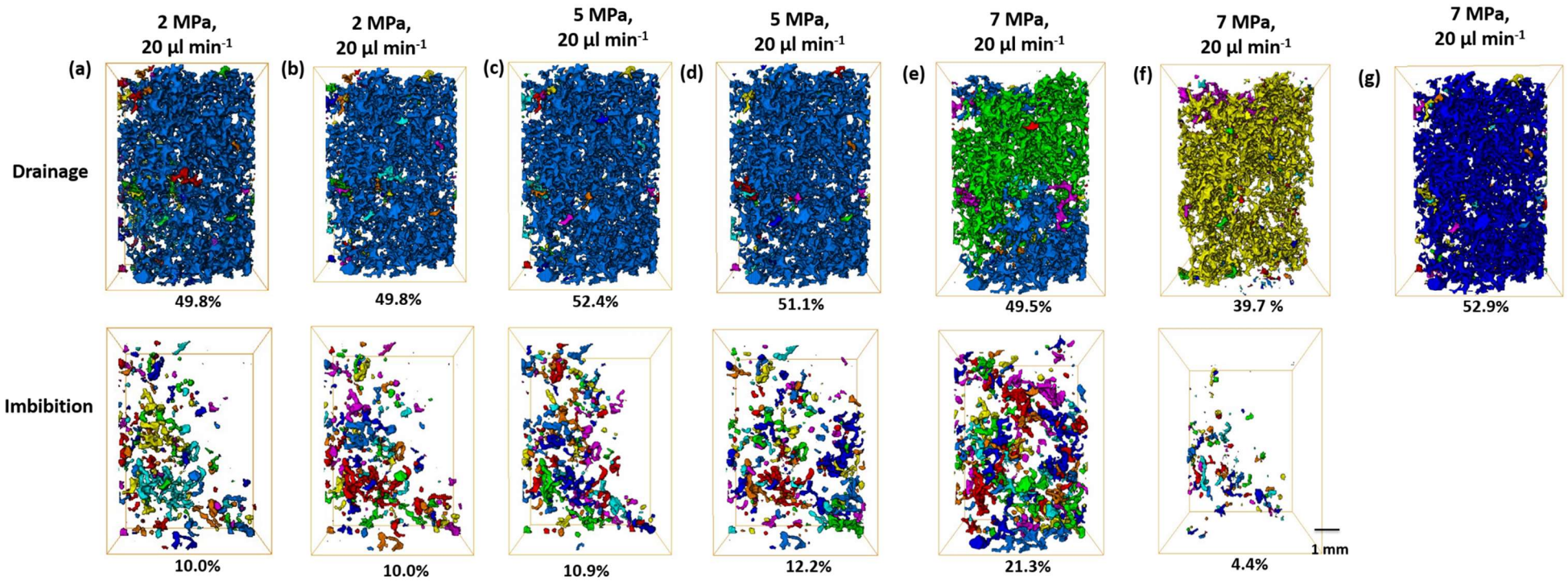

Figure 24. 3D rendering of H_2 clusters with saturation percentages in experiments. Discrete clusters were rendered in colours, where mainly one colour marks one large, connected cluster and different colours indicate several, not connected clusters. (a-g) Effect of pore fluid pressure on H_2 clusters and saturation after drainage and after primary imbibition. (a-b) 2 MPa, (c-d) 5 MPa and (e-g) 7 MPa, all at a constant flow rate of 20 µl min^{-1} corresponding to capillary numbers of 1.7x10^{-8} and 2.4x10^{-6}, respectively. Large, connected clusters that existed after drainage were broken down to numerous smaller clusters after imbibition, with apparently no clear relationship between H_2 saturation and pore fluid pressure (Thaysen et al., 2022).

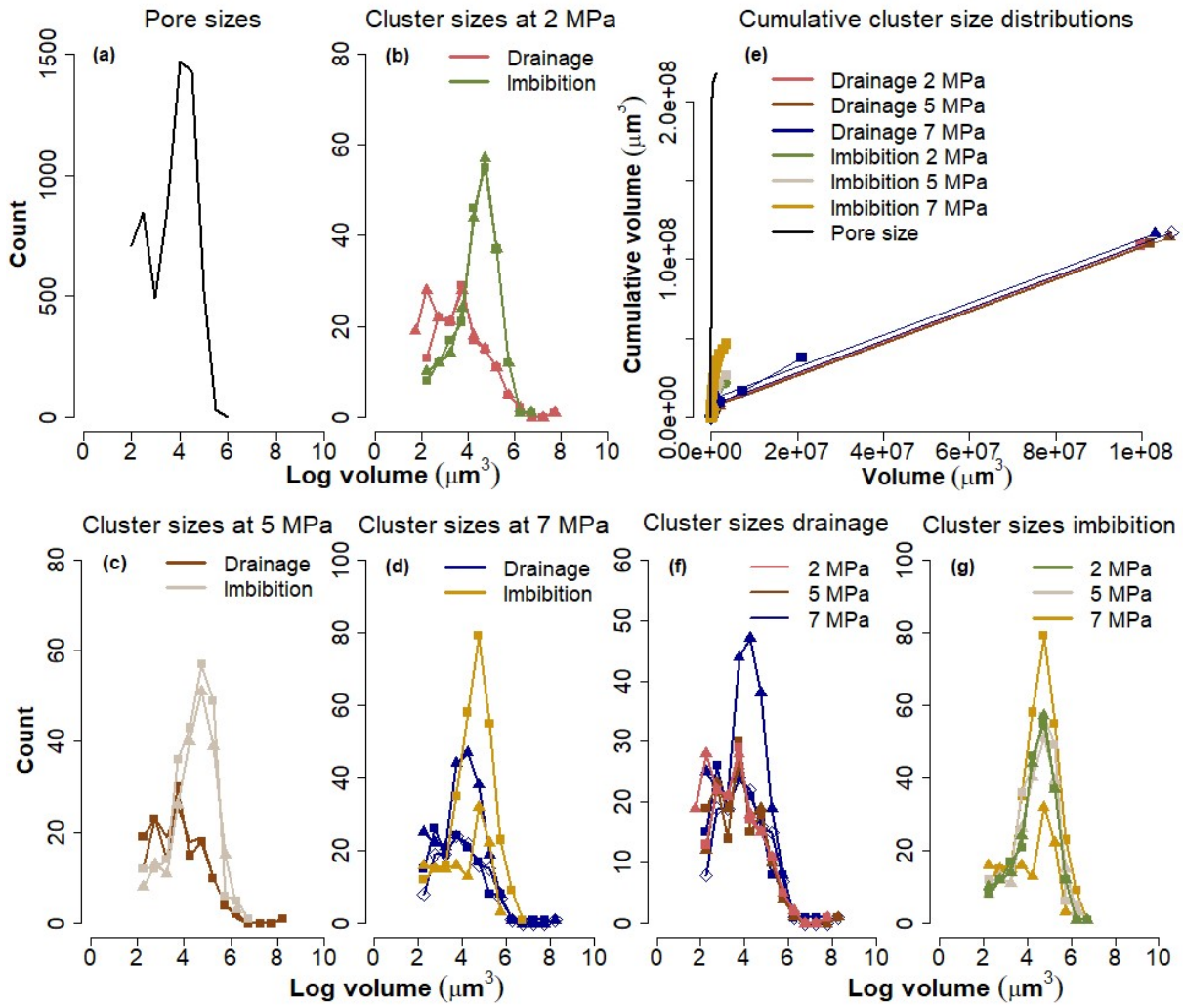

Figure 25. (a) Pore size distribution as derived from the micro-CT image of the water-saturated rock. Hydrogen cluster size distributions after drainage and imbibition in experiments at 20 µl min^{-1} flowrate and pore fluid pressures of 2 MPa (b), 5 MPa (c) and 7 MPa d), and cumulative pore size and H_2 cluster size (CS) distributions at different pore fluid pressures (e), where squares, triangles and rhombi mark the distinct repeat experiments. (f) Hydrogen cluster size distribution after drainage for all experiments and (g) Hydrogen cluster size distribution after imbibition for all experiments. Note the large H_2 clusters of ~10^8 µm^3 that exist after drainage in (b)-(d). A decrease in the biggest cluster volume after imbibition in (b)-(d) along with an increase in the number of small clusters marks the change in H_2 structure during the drainage and imbibition processes. Histogram plots in (a)-(d), (f) and (g) used a bin size of 10 (Thaysen et al., 2022).

6.2.3 Comparison to nitrogen

The N_2 saturation was similar to the H_2 saturation during drainage (48.7% vs. 51.7 ± 0.66 %, respectively) but N_2 saturation after brine imbibition was much higher (33.9 % vs. 11.5 ± 0.64 %, respectively; Figure 26). The N_c of H_2 and N_2 during drainage were 1.7×10^{-8} and 3.5×10^{-8}, respectively.

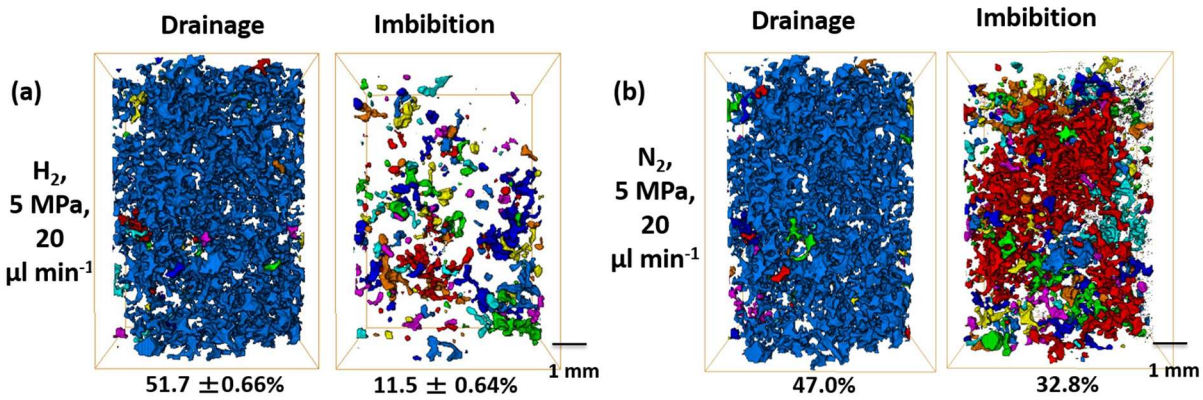

Figure 26. Nitrogen clusters and saturations during drainage and imbibition at 5 MPa pore fluid pressure and a flowrate of 20 µl min^{-1}.

6.3 Discussion

6.3.1 Hydrogen flow behaviour and trapping mechanisms

Hydrogen behaved as a non-wetting phase, filling the centre of the pores, with residual brine in the pore corners and throats (Figure 23b and c), indicating a water wetting system. The largest H_2 cluster was much larger than discrete pores at any pore fluid pressure during drainage (Figure 25), indicating a good connectivity of the H_2 (Singh et al., 2017). Hydrogen trapping occurred via snap-off of H_2 ganglia (Figure 27). The process of displacing a non-wetting fluid by a wetting fluid in porous media can occur in two different ways. One way is called "piston-like displacement," which involves the wetting fluid filling up the pore space like a piston and pushing the non-wetting fluid out. The other way is called "snap-off," which occurs when the wetting fluid swells in the corner layers of a pore throat during the water invasion of water-wet porous rocks. This process continues until the threshold capillary pressure is exceeded, causing the throat to spontaneously fill with water and disconnecting the non-wetting phase. If snap-off occurs, it can lead to the trapping of the non-wetting fluid (Singh et al., 2017; Krevor et al., 2015). Brine films around grains were not directly visible in the tomographic images (Figure 23b and c) but were revealed by subtraction of the water-saturated scan from the brine-saturated scan after H_2 injection, following the registration of the brine-saturated scan after H_2 injection to the water-saturated scan (Figure 23d and e). Figure 23d and Figure 23e suggest that brine films were discontinuous and very thin.

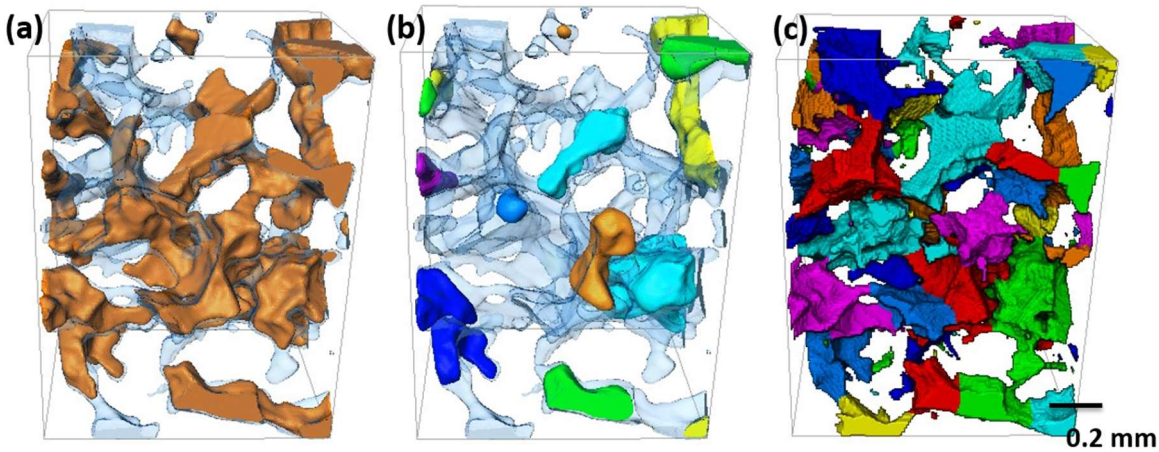

Figure 27. Example of a snap-off event. (a) Labelled H_2-filled volume after drainage (orange), spanning over several pores, and total pore space (transparent blue) showing one large interconnected H_2-filled pore volume. (b) Labelled H_2-filled volume after brine imbibition (different coloured shades) and the total pore space (transparent blue) showing several, not connected H_2 ganglia and the snapped-off H_2 droplet (cobalt blue) in the centre, left hand side. (c) Pore body visualisation of the same volume (Thaysen et al., 2022).

6.3.2 Effect of pore fluid pressure

We observed no dependence of the H_2 saturation during drainage on pore fluid pressure, considering that 2 out of 3 experiments at 7 MPa showed the same H_2 saturation of ~50 % as at 2 and 5 MPa (Figure 24). The one experiment at 7 MPa which had only 39.7 % H_2 saturation (Figure 24f and blue triangles in Figure 25f) did also not have the same H_2 cluster size distribution as the remaining experiments (Figure 25f), despite using the same experimental settings as for all other experiments at 7 MPa, and the log archives of the pore fluid pressures and injected volumes revealed no abnormalities. A shift in the distribution of cluster sizes can indicate a change in wettability, regardless of the measured H_2 saturation. Yet, as two of the results at 7 MPa showed a similar distribution as at the other pressures, it seems likely that this experiment is an outlier. The experiment was acquired after a filament change on the µCT apparatus, which implied that a slightly different part of the same rock core was imaged (13.6 % vs. 12.5 % porosity). Yet, in principle this should not have affected the results significantly, and subsequent experiments did return to show ~50 % H_2 saturation, e.g. the H_2 stability experiment (Figure 23).

The observed constant drainage H_2 saturations with increasing pore fluid pressures from 2 to 7 MPa are in line with a lack of a dependence of the H_2 wettability on pressure increases from 2-10 MPa in Berea and Bentheimer sandstone (Hashemi et al., 2021), with only very small increases of ~3-6° in the H_2 contact angles at pressure increases from 2 to 7 MPa in Basalt (Al-Yaseri and Jha, 2021) and clay (Al-Yaseri et al., 2021) and quartz (Iglauer et al., 2021), and with previous findings of no change in the characteristic trapping curves for CO_2 and N_2 at a wide range of pressure and temperature conditions (Niu et al., 2015). The general anticipation of an increase in gas saturation with injection pressure (Thomas et al., 1968; Boone et al., 2014) may still be valid over pressure ranges larger than the one investigated here. At unchanged wettability, the S_{nwi} is controlled by the capillary pressure which in turn is controlled either by the fractional flow (during simultaneous injection) or by the viscous force pressure drop (during single fluid phase injection). Thus, the independence of the S_{nwi} from the pore fluid pressure indicates that the viscous pressure drop is not being significantly altered by the changing pressure, e.g. the H_2 viscosity change is not having a major impact on the force required to drive flow. Significant loss of H_2 from the gas phase at higher pressures by

dissolution into the brine is precluded by the low solubility of H_2 of ~0.02 mol kgw^{-1} at 2.5 MPa (Lucia et al., 2015). The H_2 stability experiments showed that H_2 saturation at 5 MPa did not change over a time period of ten hours (49.55 % at time zero vs. 49.53 % ten hours after; Figure 23), evidencing a stable result and no H_2 loss by dissolution. Recent reports of a significantly increased S_{nwr} when using H_2-equilibrated brine over non H_2-equilibrated brine in H_2 and brine displacement experiments in Bentheimer sandstone at 10 MPa and 50 °C (Al-Yaseri et al., 2022), indicate that employing a combination of high temperature and pressure causes significant dissolution of H_2.

Looking at the S_{nwr} data, only (Figure 24), there was no clear dependency on pore fluid pressure during imbibition. Any change may, however, have been masked by the high variation between the two results at 7 MPa (4-21 % Figure 24e-g). Considering that the experiment at 7 MPa with the low S_{nwi} of 40 % could be identified as an outlier (see the discussion in the beginning of section 4.3.2, and Figure 25f, blue triangles) and that the S_{nwr} is a function of the S_{nwi} where a lower S_{nwi} will tend to overestimate recovery (Herring et al., 2013; Blunt, 2017), we may disregard the S_{nwr} of 4 %. The large increase in trapped H_2 in the second full primary drainage and secondary imbibition experiment at 7 MPa (Figure 24e) was probably due to the poorer initial H_2 connectivity (Herring et al., 2013). The H_2 cluster size distribution for this experiment showed an increase in the number of intermediate size clusters compared to the other experiments (Figure 25g, dark yellow squares), without however shifting the cluster distribution, suggesting no wettability change. This indicates that variation in one or more of the other thermophysical properties –density, viscosity, or IFT – have resulted in the impact on the pore scale fluid configuration. Meanwhile, a poorer initial H_2 connectivity was not confirmed by the third repetition of primary drainage at 7 MPa (Figure 24g). More experiments at 7 MPa are needed to confirm the result of increased trapping at higher pore fluid pressures.

Given a hydrostatic gradient of ~10 MPa/km an increase of the S_{nwr} with increasing pore fluid pressure, as suggested by the second experiment at 7 MPa (Figure 24e), would indicate that from a recovery perspective, deeper aquifers are less favourable for H_2 storage operations. However, unlike our unsteady state experiments which showed barely any pressure difference between inlet and outlet, in a real H_2 storage operation, the well pressure is higher than the reservoir pressure and the brine is not injected, but naturally flowing into previously H_2-saturated rock when the H_2 is recovered, again due to a pressure difference. Our displacement study results are hence applicable to the fringe of the H_2-saturated zone, only, where pressure differences are very small. A decreased H_2 recovery with depth would not align well with other criteria for an economical and safe H_2 storage operation, such as a lower cushion gas requirement with elevated depth (Heinemann et al., 2018) and reduced risks for H_2-linked microbial activity at higher depths due to higher temperatures (Thaysen et al., 2021).

The S_{nwr} of 10-21 % was significantly lower than the previously reported H_2 S_{nwr} of 41 % for a Gosford sandstone under ambient conditions (Jha et al., 2021) but in line with 20-25 % H_2 S_{nwr} in a Bentheimer sandstone at 10 MPa and 50 °C (Jangda et al., 2022). As mentioned previously, the short length rock sample in Jha et al. (2021) suggests that their results were affected by capillary end effects (Pak, 2014). However, the relatively high bulk N_C of 2.3-2.4x10^{--6} during brine imbibition in our experiments and those of Jangda et al. (2022) may have mobilised more residual H_2 than under strict capillary regime conditions. Our results are higher than previously reported S_{nwr} of <2 % in a Fontainebleau sandstone at 0.4 MPa, ambient temperature and bulk Nc of 3.5*10^{-8} (Al-Yaseri et al., 2022), however the S_{nwi} in this study was extremely low (4 %).

6.3.3 Comparison to nitrogen

The N_2 saturation was comparable to the H_2 saturation during drainage at similar N_C of 1-3x10^{-8} but the S_{nwr} after imbibition was ~20 % higher for N_2 than for H_2 (Figure 26). Using N_2 as a proxy for H_2 in experimental drainage and imbibition studies is hence not advisable. Considering the high degree of N_2 trapping, the use of N_2 as a cushion gas for H_2 storage operations which could reduce operational costs seems favourable (Heinemann et al., 2021). Our results are lower than a reported 64 % N_2 S_{nwi} after drainage and 43 % N_2 S_{nwr} in a Berea sandstone (20-22 % porosity) at 5.5 MPa and 20°C (Khishvand et al., 2016), and higher than 43 % N_2 S_{nwi} in a Bashijiqike tight sandstone (5.6 % porosity) at 8 MPa and ambient temperature (Cao et al., 2019). The trend in the differences of the N_2 saturation in the above studies follows the same trend as the differences in the porosities of the studied sandstones, with the Clashach sandstone (14 % porosity) being intermediate between the two other rocks. This indicates that porosity differences between the different rock types applied in the above experiments defined the observed N_2 saturations, yet differences in the pore throats dimensions may equally have contributed or caused this. It also suggests that S_{nwi} and S_{nwr} depend strongly on (the local conditions within) each rock, and that these rock type/local effects may mask any effect of injection conditions, whereas trends in the rock-specific behaviour will be controlled by pressure and flow conditions. Meanwhile observations of N_2 S_{nwi} and S_{nwr} of 15-26 % and 8-17 %, respectively, in a Fontainebleau sandstone with 9.7 % porosity at 0.4 MPa, ambient temperature and Nc of 3.5x10^{-8} to 7x10^{-7} do not confirm the relation between initial and residual saturations and porosity (Al-Yaseri et al., 2022). This suggests that other parameters such as the absolute permeability of a rock also shape the rock specific response to N_2 and brine displacement processes. More studies on different types of rock and under similar injection conditions are needed to better understand the rock-specific differences in S_{nwi} and S_{nwr}.

7 Application of experimental results in numerical reservoir simulations

The performed experiments allow a more accurate prediction of the flow processes on a larger scale. Here, numerical simulations on field scales are an established method to match and forecast the operation of gas storages allowing the process to be optimized. The following presents the workflow from the laboratory to input parameters for numerical simulations.

7.1 Molecular diffusions coefficients

Before the experimental data can be built into the simulator, a more general characterization of the molecular diffusion has to be developed. Generally, the diffusive flux in reservoir simulators is described as follows:

$$F_D^k = -\rho_{m,g} \cdot D_{pm}^k \cdot \nabla c_g^k$$

where F_D^k is the diffusive flux in $mol/(m^2 \cdot s)$, $\rho_{m,g}$ is the molar density of the gaseous phase in mol/m^3, D_{pm}^k is the diffusion coefficient of component k in the porous media in m^2/s , and c_g^k is the mole fraction of component k in the gaseous phase.

Considering a system composing two components, the effective binary diffusion coefficient is typically modelled during numerical simulation based on the following relationship:

$$D_{pm}^{AB} = \phi \cdot \tau \cdot S_g \cdot D^{AB}$$

where ϕ is the porosity, τ is the tortuosity factor of the porous medium, S_g is the gas saturation and D^{AB} is the binary diffusion coefficient in m^2/s .

Here, the experimental results are used to establish a model describing the molecular diffusion in rock samples at storage conditions. Existing models of binary diffusion coefficients are often limited to ambient to low pressures and temperatures. Therefore, a model with the following relationship is developed:

$$D_{pm}^{AB}(p, T, \phi, k, S_g) = \phi \cdot S_g \cdot \tau(\phi, k, S_g) \cdot D^{AB}(p, T)$$

In general, the modelling approach can be divided into two parts: 1) the development of a correlation describing the tortuosity factor based on various samples with varying properties at the same temperature and pressure conditions; 2) the establishment of correlation to predict binary diffusion coefficients of methane-hydrogen independently of the porous medium with changing temperature and pressure. The correlation based on the petrophysical properties is shown in Figure 28.

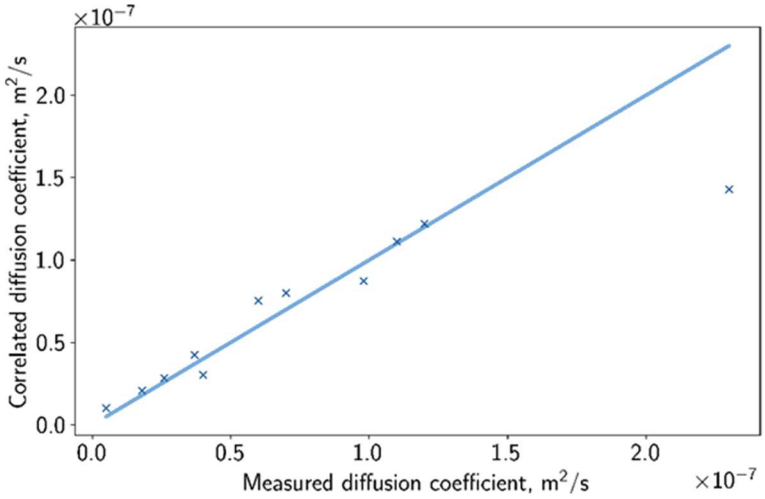

Figure 28. Correlation of diffusion coefficient based on various rock samples varying in petrophysical properties and saturation at reference conditions (100 bar, 40 °C)

A proper match, indicated by correlated values close to the identity line, was achieved with the following empirical relationship:

$$D_{pm}^{AB} = \phi^2 \cdot S_g^2 \cdot k_{\text{eff}}^{\frac{1}{5}} \cdot 3.4 \cdot 10^{-4}\, m^2 / \left(m^{\frac{2}{5}} \cdot s\right)$$

where the porosity and saturation are given in fractions and the effective permeability in m^2. The Fullers method (Fuller et al., 1969) was selected due to its reported good accuracy at lower pressure and temperatures and evaluated at T= 40°C and P=10 bar to obtain a reference bulk diffusion coefficient. With this reference value, the samples' tortuosity factor can be determined, leading to the general formulation:

$$D_{pm}^{AB} = \phi \cdot S_g \cdot \tau \cdot D^{AB}$$
$$\tau = \phi \cdot S_g \cdot k_{\text{eff}}^{\frac{1}{5}} \cdot 176.916\, m^{-\frac{2}{5}}$$

Next, a correlation for the binary diffusion coefficient was constructed. A polynomial regression second degree (2x2y) was used to describe the effective diffusion coefficient (measured) in dependency of pressure and temperature (See Figure 29).

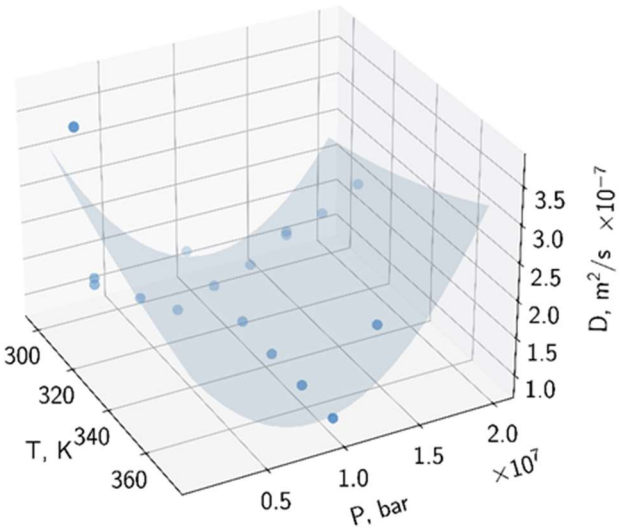

Figure 29. Effective diffusion coefficient in dependency of pressure and temperature of the Bentheimer Sandstone sample – dotted: experimental data; surface: polynomial regression

Using the first correlation, the polynomial function can be transformed, allowing the characterization of the binary diffusion coefficient. Here, the following parameters were achieved:

$$D^{AB}(T,p) = \beta_1 + \beta_2 \cdot T + \beta_3 \cdot p + \beta_4 \cdot T^2 + \beta_5 \cdot T \cdot p + \beta_6 \cdot p^2$$

$$\beta_1 = 3.61069 \cdot 10^{-5}\ m^2/s \qquad \beta_4 = 1.67793 \cdot 10^{-10}\ m^2/(s \cdot K^2)$$
$$\beta_2 = -1.46672 \cdot 10^{-7}\ m^2/(s \cdot K) \qquad \beta_5 = 2.95155 \cdot 10^{-15}\ m^2/(s \cdot K \cdot Pa)$$
$$\beta_3 = -1.74842 \cdot 10^{-12}\ m^2/(s \cdot Pa) \qquad \beta_6 = 3.71863 \cdot 10^{-20} m^2/(s \cdot Pa^2)$$

This function was fitted to the measured effective diffusion coefficients with the Bentheimer sandstone sample at various conditions. To extend the region of validity three additional measurements were conducted (10bar/40°C, 20bar/40°C, 150bar/85°C). The measurements with the storage site samples under reference and storage conditions were used as a test set to assess the developed correlations' accuracy. Table 7 presents the results of this comparison.

Table 7. Overview of relative errors of the correlation regarding the test set

Exp. no	Sample	T [°C]	P [bar]	Measured diff. coeff. [m²/s]	Correlated diff. coeff. [m²/s]	Relative error [%]
1	Chattian sand	40	100	$7.00 \cdot 10^{-8}$	$8.00 \cdot 10^{-8}$	-14.3
2	Chattian sand	50	106	$6.50 \cdot 10^{-8}$	$7.55 \cdot 10^{-8}$	-16.2
3	Aquitanian formation	40	100	$6.00 \cdot 10^{-8}$	$7.54 \cdot 10^{-8}$	-25.7
4	Aquitanian formation	25	53.5	$1.10 \cdot 10^{-7}$	$1.32 \cdot 10^{-7}$	-19.8
5	Pliocene sand	40	100	$2.30 \cdot 10^{-7}$	$1.43 \cdot 10^{-7}$	37.9
6	Pliocene sand	45	88.3	$2.00 \cdot 10^{-7}$	$1.48 \cdot 10^{-7}$	26.1
7	Ebes fm.	40	100	$2.60 \cdot 10^{-8}$	$2.84 \cdot 10^{-8}$	-9.4

8	Ebes fm.	107	140.5	$1.70 \cdot 10^{-8}$	$4.22 \cdot 10^{-8}$	-148.3
9	Ujfalu fm.	40	100	$1.20 \cdot 10^{-7}$	$1.22 \cdot 10^{-7}$	-1.7
10	Ujfalu fm.	86	116.5	$1.10 \cdot 10^{-7}$	$1.22 \cdot 10^{-7}$	-10.8
11	Detfurth formation	40	100	$9.80 \cdot 10^{-8}$	$5.55 \cdot 10^{-8}$	43.3
12	Detfurth formation	96	287.25	$1.70 \cdot 10^{-7}$	$4.32 \cdot 10^{-7}$	-153.9
13	Rough Rotliegendes	40	100	$1.80 \cdot 10^{-8}$	$2.09 \cdot 10^{-8}$	-16.0
14	Rough Rotliegendes	92	203	$9.00 \cdot 10^{-9}$	$6.51 \cdot 10^{-8}$	-623.1

In general, the reproducibility shows a good accuracy with less than 50 %, with some exceptions. Remarkable are experiments 8, 12, and 14, where the relative error is higher than 100 %. The remarkable deviations were samples measured at the experimental matrix's higher boundaries and exceeding these conditions. Furthermore, the binary diffusion coefficient is overestimated for these cases; therefore, the process is more substantial than observed. Regarding the significant deviation of 623% for the Rough Rotliegendes sample, the temperature is located at the upper boundary, the pressure exceeds the upper limit, and the permeability is the lowest of the entire measurement series. In this region, the established correlation seems to be inaccurate, leading to a higher error. Nevertheless, the established correlation allows the reproduction of the observed molecular diffusion coefficients for sandstone samples in a pressure and temperature range of 10 to 200 bar and 25 to 100°C.

The developed correlations can be implemented into numerical simulators to predict the mixing effects during hydrogen storage in the subsurface. However, many commercial simulators are limited in their level of adaption, and only the binary diffusion coefficient can be implemented. Here, the presented modelling has to be modified. Further, additional measurements with different gas components, such as carbon dioxide or nitrogen, could lead to a more general model instead of a polynomial regression.

7.2 Mechanical dispersivities

Only a few commercial reservoir simulators (e.g. CMG GEM) allow to consider a flow velocity dependent dispersive flux. DuMu^x allows to consider Scheidegger's relations for dispersion when a vertex-centered finite volume method (box method) is used as spatial discretization scheme (Huber and Helmig, 2000). This in turn only works when a conforming grid is used. The box method uses a finite element approach to determine the fluxes, which allows to obtain the complete flux vector at each integration point. Based on this vector the mean flow direction and velocity can be determined and the dispersion tensor can be calculated. In contrast the two-point flux approximation which is usually applied on corner-point grids (typical grid in petroleum reservoir simulation) only allows to determine the fluxes perpendicular to each face and the mean flow velocity and direction cannot be determined straight forward.
As discussed in section 4.3 the experimental results show that dispersive mixing can be modeled sufficiently good by using a constant value for the dispersivity. Still it has to be considered that the dispersivity is dependent on the length scale and that it is a spatial parameter and might have a different value in each grid cell of a reservoir simulation model.
Dispersivity has to be defined on the scale of the flow problem. Hence, in a reservoir simulation model the value(s) for dispersivity have to be defined on reservoir scale. In the laboratory experiments we tried to go to the maximum possible scale which was in this case 25 m. This length scale might be similar to the scale of a field trial with only a small amount of hydrogen

injection and consequently only a low spreading of hydrogen around the storage well. For a large hydrogen storage in operation the length scale of the flow problem is probably 10 to 1000 times larger and consequently also the dispersivity is expected to be higher. Investigations of the influence of scale on dispersivity have shown a nearly linear trend (Gelhar et al., 1992). This trend also coincides with the summary in Table 2.
The dependency of the dispersivity on the porous medium characteristics was not investigated in this study. Therefore, no conclusions can be drawn on potential spatial variations in dispersivity. It has to be considered that real reservoirs are much more heterogeneous than the filling of the slim tube what consequently leads to a higher dispersivity.
For a simulation study in a very homogeneous reservoir we propose the following law which is based on the mean value of our measurements:

$$\alpha_L = 0.04\,\frac{L}{25}$$

where L is the characteristic length scale of the flow problem. When a good match of the observed data (e.g. the withdrawn gas composition from storage wells) cannot be obtained with a homogenous dispersivity it is proposed to adjust the dispersivity in the simulation model per region or layer.

7.3 Relative permeability curves

While dispersion and diffusion mainly affect the flux of different components, the relative permeabilities impact the flow of the phases (e.g. gas and water) in porous media. Here, this transport process is covered by Darcy's law for multiphase flow:

$$u_i = -\frac{K \cdot k_{ri}}{\mu_i}\,(\nabla p_i - \hat{\rho}_i g)$$

Where u_i is the Darcy velocity in m/s, K is the absolute permeability in m², k_{ri} is the relative permeability of phase i, μ_i is the dynamic viscosity of phase i in $Pa \cdot s$, ∇p_i is the pressure gradient in Pa/m, $\hat{\rho}_i$ is the density of phase i in kg/m³ and g is the gravity acceleration in m/s².

Within numerical simulations of multiphase flow in porous media, Darcy's law represents the advective term of the advection-diffusion-equation, where the relative permeability curves are a typical and crucial input parameter. Usually, established models (e.g. Brooks-Corey) but also tabulated curves can be imported, and no specific changes in the models have to be performed. Nevertheless, also exceptional cases such as hysteresis are typical options. The relative permeability curves developed based on the experimental investigations are provided as tables and modified Corey functions in deliverable D4.3 (Michelsen et al. (2023)).

8 Conclusions and perspectives

The flow behaviour of hydrogen in underground reservoirs was investigated by measurements of effective molecular diffusion and mechanical dispersion for the binary system H_2-CH_4, as well as by the determination of relative permeability curves for the hydrogen-brine system under reservoir conditions.

Molecular diffusion

- Diffusion rates for the binary system H_2-CH_4 were measured on eight different rock samples including samples from gas storage sites in Europe. Based on the results, effective diffusion coefficients were determined by comparing the measured data with a numerical simulation model.
- In total 29 diffusion measurements were carried out. Among all diffusion measurements, the values for the effective diffusion coefficient range from $5 \cdot 10^{-9}$ to $2.3 \cdot 10^{-7}$ m²/s.
- The influence of pressure, temperature and water saturation was investigated using a Bentheimer sandstone as reference sample. The plotting of the effective diffusion coefficients versus pressure, temperature and water saturation show clear trends, which, however, are partly different than calculated by conventional correlations. The measurements indicate deviations from the correlations at pressures above 75 bar, where the effective diffusion coefficient increases with increasing pressure. For the dependence on temperature at 100 bar the measurements also do not reflect the correlation as the values decrease when increasing the temperature. The decreasing trend of the effective diffusion coefficient with increasing water saturation fits to the expectation. The comparion of effective diffusion coefficient for the different samples at reference conditions show the general trend that the effective diffusivity increases with porosity and permeability.

Mechanical dispersion

- The mechanical dispersivity for the binary system H_2-CH_4 was measured by using a slim tube coil with a length of 25 m. In total 13 dispersion measurements were carried out for which pressure, temperature and flow velocity were varied. The determined longitudinal dispersivities lie between 0.018 and 0.060 m.
- The measurements show that the dispersivity is not independent of pressure, temperature and flow velocity. Nevertheless, the results of this study show that Scheidegger's theory for dispersion allows to predict dispersive mixing between two gases under subsurface storage conditions sufficiently good. However, it can be recognized that there are some effects which are not captured by this law. The strong sensitivity to pressure suggests that fluid properties such as density and viscosity have an influence on the dispersivity.

Relative permeability

- The experiments on the H_2 relative permeability showed that the rock type (i.e., pore structure and porosity) had the greatest influence on H_2 relative permeability, where increases in porosity resulted in increases in the H_2 relative permeability. Increasing pressure at higher hydrogen saturations, increased the H_2 viscosity and as such reduced its relative permeability, indicating that from an injectivity and recovery perspective higher pressure, i.e. deeper reservoirs are less favourable for H_2 storage. Salinity had only a small effect on the relative permeability of H_2, where increasing salinity caused a reduction in relative permeability, which may be due to the increase

in IFT with increasing salinity. A comparison of the shapes of the H_2, N_2 and CH_4 relative permeability curves suggested higher injectivity and recovery of H_2 and N_2 over CH_4.

- The µCT experiments on H_2 injectivity and recovery showed no clear influence of pore fluid pressure on H_2 saturation in the investigated pressure range of 2-7 MPa, with ~50% of the pore space saturated with H_2 during drainage at all pressures. However, during imbibition 20%, 22% and 43% of the initial was H_2 trapped at 2, 5 and 7 MPa, respectively, at a capillary number of 2.4×10^{-6}, again indicating that deeper reservoirs are less favourable for H_2 storage from a H_2 recovery perspective.
- The drainage relative permeability curves showed good similarity between H_2 and N_2. The µCT experiments confirmed that the saturation after drainage was similar for H_2 and N_2, however the saturation after imbibition was significantly higher for H_2 than for N_2. The difference in displacement behaviour during drainage and imbibition can be explained with a predominance of buoyancy and capillary forces acting during drainage, and with gravitational and capillary forces dominating the imbibition process (see section 3.2.5). This highlights the importance of measuring relative permeability curves for both drainage and imbibition, and is supported by previous findings of relative permeability hysteresis (Lysyy et al., 2022b; Boon and Hajibeygi, 2022). Based on the combined results, we do not recommend using N_2 as an analogue for H_2.
- The finding of a higher CH_4 relative permeability over H_2 and N_2 was not expected based on the experimental conditions and fluid flow properties of the gases.
- The drainage relative permeability experiments suggested that pressure has a significant impact on wettability at pressure increases from 0.1 MPa to 10.34 MPa. The µCT experiments indicated no change of wettability with a pressure increase from 2 to 7 MPa during neither drainage nor imbibition. Based on the experimental conditions and the expected driving forces behind the fluid displacements, a pressure effect was not anticipated during drainage but could be explained by a higher viscosity of H_2 at higher pressure.
- The maximum gas saturations in the drainage relative permeability experiments were similar at 0.1 MPa and 10.34 MPa, in line with no change in the gas saturations during drainage at pressure increases from 2 to 7 MPa in the µCT experiments.
- It has been postulated that the low viscosity of H_2 will cause the gas to travel swiftly, making it unsuitable for displacing brine and causing low H_2 injectivity (Chaturvedi et al., 2022). The combined results from µCT experiments and relative permeability experiments showed that, from an injectivity and recovery perspective, a variety of porous rocks are suitable for underground H_2 storage. In addition, both experimental studies suggest that from a gas recovery perspective shallower, i.e. lower pressure sites, are recommended for future H_2 storage operations in porous media.
- Results from dynamic H_2 and brine cyclic injection experiments using a synchrotron light source are underway and are expected to further insight into displacement mechanisms.
- Further relative permeability studies that use visualization of the fluid flow inside the core are recommended to explain all experimental findings.

The results from our experiments could be fed into large-scale reservoir simulators to improve geological hydrogen storage planning by reducing the uncertainties surrounding prediction of hydrogen flow in subsurface. To do so data sets were developed which can be used as input parameters for simulation models:

- For the effective diffusion coefficients a two stage correlation was constructed by least square fitting. The first stage correlates the bulk binary diffusion coefficient dependent on pressure and temperature. In the second stage the effective porous medium

diffusion coefficient is correlated dependent on porosity, permeability and gas saturation.

- A scale dependent law for the mechanical dispersivity is provided based on the experimental results which can be used as an initial guess.
- The relative permeability curves are provided as tables. Modified Corey functions were fitted to the measured data which can be used alternatively.

9 References

Al-Yaseri, Ahmed; Esteban, Lionel; Giwelli, Ausama; Sarout, Joel; Lebedev, Maxim; Sarmadivaleh, Mohammad (2022): Initial and residual trapping of hydrogen and nitrogen in Fontainebleau sandstone using nuclear magnetic resonance core flooding. *International Journal of Hydrogen Energy* 47 (53), pp. 22482–22494.

Al-Yaseri, Ahmed; Jha, Nilesh Kumar (2021): On hydrogen wettability of basaltic rock. *Journal of Petroleum Science and Engineering* 200, p. 108387.

Al-Yaseri, Ahmed; Wolff-Boenisch, Domenik; Fauziah, Cut Aja; Iglauer, Stefan (2021): Hydrogen wettability of clays: Implications for underground hydrogen storage. *International Journal of Hydrogen Energy* 46 (69), pp. 34356–34361.

Andrew, Matthew; Bijeljic, Branko; Blunt, Martin J. (2014): Pore-scale imaging of trapped supercritical carbon dioxide in sandstones and carbonates. *International Journal of Greenhouse Gas Control* 22, pp. 1–14.

Bear, Jacob (2013): Dynamics of Fluids in Porous Media. Reprint. Originally published: New York: American Elsevier. Pub. Co., 1972. Originally published in series: Environmental science series (New York, 1972-). With corrections. New York: Dover Publ.

Bear, Jacob (2018): Modeling phenomena of flow and transport in porous media. Cham: Springer (Theory and applications of transport in porous media, volume 31).

Blunt, Martin J. (2017): Multiphase Flow in Permeable Media: Cambridge University Press.

Boon, Maartje; Hajibeygi, Hadi (2022): Experimental characterization of Formula: see text/water multiphase flow in heterogeneous sandstone rock at the core scale relevant for underground hydrogen storage (UHS). *Scientific reports* 12 (1), p. 14604.

Boone, M. A.; Kock, T. de; Bultreys, T.; Schutter, G. de; Vontobel, P.; van Hoorebeke, L.; Cnudde, V. (2014): 3D mapping of water in oolithic limestone at atmospheric and vacuum saturation using X-ray micro-CT differential imaging. *Materials Characterization* 97, pp. 150–160.

Buades, A.; Coll, B.; Morel, J.-M. (2005): A Non-Local Algorithm for Image Denoising. *2005 IEEE Computer Society Conference on Computer Vision and Pattern Recognition (CVPR'05)*, pp. 60–65.

Cao, Qian; Gong, Yanjie; Fan, Tailiang; Wu, Jun (2019): Pore-scale simulations of gas storage in tight sandstone reservoirs for a sequence of increasing injection pressure based on micro-CT. *Journal of Natural Gas Science and Engineering* 64, pp. 15–27.

Carriere, J. F.; Fasanino, G.; Tek, M. R. (1985): Mixing in Underground Storage Reservoirs. In : All Days. SPE Annual Technical Conference and Exhibition. Las Vegas, Nevada, 22.09.1985 - 26.09.1985: SPE.

Chaturvedi, Krishna Raghav; Bajpai, Sushant; Trivedi, Japan; Sharma, Tushar (2022): Air Foams for Mobility Control and Subsurface Storage of Hydrogen in Porous Media: An Experimental Study. *Energy & Fuels* 36 (9), pp. 5036–5046.

Chen, Lillian Lung-yu; Katz, Donald L.; Tek, M. Rasin (1977): Binary gas diffusion of methane-nitrogen through porous solids. *AIChE Journal* 23 (3), pp. 336–341.

Chow, Y. FlorenceT.; Maitland, Geoffrey C.; Trusler, J. MartinP. (2018): Interfacial tensions of (H2O + H2) and (H2O + CO2 + H2) systems at temperatures of (298–448) K and pressures up to 45 MPa. *Fluid Phase Equilibria* 475, pp. 37–44.

Chow, Y.T.F.; Maitland, G. C.; Trusler; J.P.M. (2020): Erratum to "Interfacial tensions of (H2O + H-2) and (H2O + CO2 + H-2) systems at temperatures of (298-448) K and pressures up to 45 MPa". *Fluid Phase Equilibria* 503(112315), p. 1.

Flesch, Steven; Pudlo, Dieter; Albrecht, Daniel; Jacob, Arne; Enzmann, Frieder (2018): Hydrogen underground storage—Petrographic and petrophysical variations in reservoir sandstones from laboratory experiments under simulated reservoir conditions. *International Journal of Hydrogen Energy* 43 (45), pp. 20822–20835.

Fuller, Edward N.; Ensley, Keith; Giddings, J. Calvin (1969): Diffusion of halogenated hydrocarbons in helium. The effect of structure on collision cross sections. *The Journal of Physical Chemistry* 73 (11), pp. 3679–3685.

Fusseis, Florian; Steeb, Holger; Xiao, Xianghui; Zhu, Wen-lu; Butler, Ian B.; Elphick, Stephen; Mäder, Urs (2014): A low-cost X-ray-transparent experimental cell for synchrotron-based X-ray microtomography studies under geological reservoir conditions. *Journal of synchrotron radiation* 21 (Pt 1), pp. 251–253.

Gelhar, Lynn W.; Welty, Claire; Rehfeldt, Kenneth R. (1992): A critical review of data on field-scale dispersion in aquifers. *Water Resources Research* 28 (7), pp. 1955–1974.

Guevara-Carrion, Gabriela; Ancherbak, Sergiy; Mialdun, Aliaksandr; Vrabec, Jadran; Shevtsova, Valentina (2019): Diffusion of methane in supercritical carbon dioxide across the Widom line. *Scientific reports* 9 (1), p. 8466.

Hashemi, Leila; Glerum, Wuis; Farajzadeh, Rouhi; Hajibeygi, Hadi (2021): Contact angle measurement for hydrogen/brine/sandstone system using captive-bubble method relevant for underground hydrogen storage. *Advances in Water Resources* 154, p. 103964.

Heinemann, N.; Booth, M. G.; Haszeldine, R. S.; Wilkinson, M.; Scafidi, J.; Edlmann, K. (2018): Hydrogen storage in porous geological formations – onshore play opportunities in the midland valley (Scotland, UK). *International Journal of Hydrogen Energy* 43 (45), pp. 20861–20874.

Heinemann, Niklas; Alcalde, Juan; Miocic, Johannes M.; Hangx, Suzanne J. T.; Kallmeyer, Jens; Ostertag-Henning, Christian et al. (2021): Enabling large-scale hydrogen storage in porous media – the scientific challenges. *Energy & Environmental Science* 14 (2), pp. 853–864.

Helmig, Rainer (1997): Multiphase flow and transport processes in the subsurface. A contribution to the modeling of hydrosysteme. Berlin, Heidelberg, New York, Barcelona, Budapest, Hong Kong, London, Milan, Paris, Santa Clara, Singapore, Tokyo: Springer (Environmental engineering).

Herring, Anna L.; Harper, Elizabeth J.; Andersson, Linnéa; Sheppard, Adrian; Bay, Brian K.; Wildenschild, Dorthe (2013): Effect of fluid topology on residual nonwetting phase trapping: Implications for geologic CO2 sequestration. *Advances in Water Resources* 62, pp. 47–58.

Ho, Clifford K.; Webb, Stephen W. (Eds.) (2006): Gas Transport in Porous Media. Dordrecht: Springer Netherlands (SpringerLink Bücher, 20).

Hogeweg, S.; Hagemann, B.; Vaccari, A.; Farahjimoghadam, F.; Moghadam, A.; Machado, C. G. et al. (2023): Integrated modeling approach for the overall performance, integrity, and durability as-sessment of hydrogen storage at the reser-voir and near-wellbore scale. *H2020 HyUSPRe project report*.

Huber, Ralf; Helmig, Rainer (2000): Node-centered finite volume discretizations for the numerical simulation of multiphase flow in heterogeneous porous media. *Computational Geosciences* 4 (2), pp. 141–164.

Ibrahim, M. N. Mohamad; Koederitz, L. F. (2001): Two-Phase Steady-State and Unsteady-State Relative Permeability Prediction Models. *SPE Middle East Oil Show*.

Iglauer, S.; Fernø, M. A.; Shearing, P.; Blunt, M. J. (2012): Comparison of residual oil cluster size distribution, morphology and saturation in oil-wet and water-wet sandstone. *Journal of Colloid and Interface Science* 375 (1), pp. 187–192.

Iglauer, S.; Paluszny, A.; Blunt, M. J. (2013): Simultaneous oil recovery and residual gas storage: A pore-level analysis using in situ X-ray micro-tomography. *Fuel* 103, pp. 905–914.

Iglauer, Stefan; Ali, Muhammad; Keshavarz, Alireza (2021): Hydrogen Wettability of Sandstone Reservoirs: Implications for Hydrogen Geo‐Storage. *Geophysical Research Letters* 48 (3).

Jangda, Zaid; Menke, Hannah; Busch, Andreas; Geiger, Sebastian; Bultreys, Tom; Lewis, Helen; Singh, Kamaljit (2022): Pore-scale visualization of hydrogen storage in a sandstone at subsurface pressure and temperature conditions: Trapping, dissolution and wettability. *Journal of Colloid and Interface Science* 629 (Pt B), pp. 316–325.

Jha, Nilesh Kumar; Al-Yaseri, Ahmed; Ghasemi, Mohsen; Al-Bayati, Duraid; Lebedev, Maxim; Sarmadivaleh, Mohammad (2021): Pore scale investigation of hydrogen injection in sandstone via X-ray micro-tomography. *International Journal of Hydrogen Energy* 46 (70), pp. 34822–34829.

Khishvand, M.; Alizadeh, A. H.; Piri, M. (2016): In-situ characterization of wettability and pore-scale displacements during two- and three-phase flow in natural porous media. *Advances in Water Resources* 97, pp. 279–298.

Krevor, Samuel; Blunt, Martin J.; Benson, Sally M.; Pentland, Christopher H.; Reynolds, Catriona; Al-Menhali, Ali; Niu, Ben (2015): Capillary trapping for geologic carbon dioxide storage – From pore scale physics to field scale implications. *International Journal of Greenhouse Gas Control* 40, pp. 221–237.

Kumar, Munish; Sok, Rob; Knackstedt, Mark; Latham, Shane; Arns, Christoph (2009): Mapping fluid distributions in 3D at the pore scale: Quantifying the influence of wettability and saturation history on rock resistivity.

Kurihara, Masanori; Liang, Jialing; Fujimoto, Fujio; Nghiem, Long; Sammon, Peter (2000): Development and Application of Underground Gas Storage Simulator. In : All Days. SPE Asia Pacific Conference on Integrated Modelling for Asset Management. Yokohama, Japan, 25.04.2000 - 26.04.2000: SPE.

Laille, J. P.; Coulomb, C.; Tek, M. R. (1986): Underground Storage in Cerville-Velaine, France: A Case History in Conversion and Inert Gas Injection as Cushion Substitute. In : SPE Annual Technical Conference and Exhibition. SPE Annual Technical Conference and Exhibition. New Orleans, Louisiana, 1986-10-05: Society of Petroleum Engineers.

Lohrenz, John; Bray, Bruce G.; Clark, Charles R. (1964): Calculating Viscosities of Reservoir Fluids From Their Compositions. *Journal of Petroleum Technology* 16 (10), pp. 1171–1176.

Lucia, Marco de; Pilz, Peter; Liebscher, Axel; Kühn, Michael (2015): Measurements of H2 Solubility in Saline Solutions under Reservoir Conditions: Preliminary Results from Project H2STORE. *Energy Procedia* 76, pp. 487–494.

Lysyy, Maksim; Ersland, Geir; Fernø, Martin (2022a): Pore-scale dynamics for underground porous media hydrogen storage. *Advances in Water Resources* 163, p. 104167.

Lysyy, Maksim; Føyen, Tore; Johannesen, Else Birkeland; Fernø, Martin; Ersland, Geir (2022b): Hydrogen Relative Permeability Hysteresis in Underground Storage. *Geophysical Research Letters* 49 (17).

Michelsen, Julia; Thaysen, Eike Marie; Hogeweg, Sebastian; Hagemann, Birger; Hassanpouryouzband, Aliakbar; Langanke, Nils et al. (2023): Data for: HyUSPRe - Work Package 4 - Hydrogen reservoir flow behaviour: Measurements of molecular diffusion, mechanical dispersion and relative permeability: GRO.data.

Millington, R. J.; Quirk, J. P. (1961): Permeability of porous solids. *Transactions of the Faraday Society* 57, p. 1200.

Mohammed, Nuhu; Abubakar, Abbas Jibrin; Enyi, Godpower Chimagwu; Ghavami, Ghasem Nasr (2019): Flow Characteristics Through Gas Alternating Gas Injection During Enhanced Gas Recovery. In : Day 3 Wed, October 23, 2019. SPE Gas & Oil Technology Showcase and Conference. Dubai, UAE, 21.10.2019 - 23.10.2019: SPE.

Nakai, T.; Sawamura, S.; Taniguchi, Y. (1995): Effect of pressure on the viscosity of aqueous cesium chloride solution at 25°C. *Journal of Molecular Liquids* 65-66, pp. 365–368.

Niu, Ben; Al‐Menhali, Ali; Krevor, Samuel C. (2015): The impact of reservoir conditions on the residual trapping of carbon dioxide in B erea sandstone. *Water Resources Research* 51 (4), pp. 2009–2029.

Pak, Tannaz (2014): Saturation tracking and identification of residual oil saturation: University of Edinburgh.

Pak, Tannaz; Butler, Ian B.; Geiger, Sebastian; van Dijke, Marinus I. J.; Sorbie, Ken S. (2015): Droplet fragmentation: 3D imaging of a previously unidentified pore-scale process during multiphase flow in porous media. *Proceedings of the National Academy of Sciences of the United States of America* 112 (7), pp. 1947–1952.

Pandey, G. N.; Tek, M. R.; Katz, D. L. (1974): Diffusion of Fluids Through Porous Media with Implications in Petroleum Geology. *AAPG Bulletin* 58.

Peng, Ding-Yu; Robinson, Donald B. (1976): A New Two-Constant Equation of State. *Industrial & Engineering Chemistry Fundamentals* 15 (1), pp. 59–64.

Pentland, C. H.; Tanino, Y.; Iglauer, S.; Blunt, M. J. (2010): Capillary trapping in water-wet sandstones: Coreflooding experiments and pore-network modeling (2). Available online at https://www.researchgate.net/publication/281764332_Capillary_trapping_in_water-wet_sandstones_Coreflooding_experiments_and_pore-network_modeling.

Perkins, T. K.; Johnston, O. C. (1963): A Review of Diffusion and Dispersion in Porous Media. *Society of Petroleum Engineers Journal* 3 (01), pp. 70–84.

Rezaei, Amin; Hassanpouryouzband, Aliakbar; Molnar, Ian; Derikvand, Zeinab; Haszeldine, R. Stuart; Edlmann, Katriona (2022): Relative Permeability of Hydrogen and Aqueous Brines in Sandstones and Carbonates at Reservoir Conditions. *Geophysical Research Letters* 49 (12).

Scheidegger, A. E. (1961): General theory of dispersion in porous media. *Journal of Geophysical Research* 66 (10), pp. 3273–3278.

Singh, Kamaljit; Menke, Hannah; Andrew, Matthew; Lin, Qingyang; Rau, Christoph; Blunt, Martin J.; Bijeljic, Branko (2017): Dynamics of snap-off and pore-filling events during two-phase fluid flow in permeable media. *Scientific reports* 7 (1), p. 5192.

Soukup, Karel; Schneider, Petr; Šolcová, Olga (2008): Comparison of Wicke–Kallenbach and Graham's diffusion cells for obtaining transport characteristics of porous solids. *Chemical Engineering Science* 63 (4), pp. 1003–1011.

Stiel, Leonard I.; Thodos, George (1961): The viscosity of nonpolar gases at normal pressures. *AIChE Journal* 7 (4), pp. 611–615.

Tek, M. R. (1989): Underground Storage of Natural Gas. Dordrecht: Springer Netherlands.

Thaysen, Eike M.; Butler, Ian B.; Hassanpouryouzband, Aliakbar; Freitas, Damien; Alvarez-Borges, Fernando; Krevor, Samuel et al. (2022): Pore-scale imaging of hydrogen displacement and trapping in porous media. *International Journal of Hydrogen Energy* 48 (8), pp. 3091–3106.

Thaysen, Eike M.; McMahon, Sean; Strobel, Gion J.; Butler, Ian B.; Ngwenya, Bryne T.; Heinemann, Niklas et al. (2021): Estimating microbial growth and hydrogen consumption in hydrogen storage in porous media. *Renewable and Sustainable Energy Reviews* 151, p. 111481.

Thomas, L. K.; Katz, D. L.; Tek, M. R. (1968): Threshold Pressure Phenomena in Porous Media. *Society of Petroleum Engineers Journal* 8 (02), pp. 174–184.

Vargaftik, Natan B. (1975): Tables on the thermophysical properties of liquids and gases. In normal and dissociated states. 2. ed. Washington: Hemisphere Publ (Advances in thermal engineering, 4).

Vlassenbroeck, J., et al (Ed.) (2010): Octopus 8: A high performance tomographic reconstruction package for X-ray tube and synchrotron micro-CT, in Advances in X-ray tomography for geomaterials. With assistance of J. Desrues, G. Viggiani, and P. Bésuelle. ISTE: London, UK.

Wicke, E.; Kallenbach, R. (1941): Die Oberflächendiffusion von Kohlendioxyd in aktiven Kohlen. *Kolloid-Zeitschrift* 97 (2), pp. 135–151.

Yang, Kaishuo; Kobeissi, Sam; Ling, Nicholas; Li, Ming; Esteban, Lionel; May, Eric F.; Johns, Michael L. (2023): Measurement of hydrogen dispersion in rock cores using benchtop NMR. *International Journal of Hydrogen Energy*.

Yekta, A. E.; Manceau, J.-C.; Gaboreau, S.; Pichavant, M.; Audigane, P. (2018): Determination of Hydrogen–Water Relative Permeability and Capillary Pressure in Sandstone: Application to Underground Hydrogen Injection in Sedimentary Formations. *Transport in Porous Media* 122 (2), pp. 333–356.

Yusibani, Elin; Nagahama, Yosuke; Kohno, Masamichi; Takata, Yasuyuki; Woodfield, Peter L.; Shinzato, Kanei; Fujii, Motoo (2011): A Capillary Tube Viscometer Designed for Measurements of Hydrogen Gas Viscosity at High Pressure and High Temperature. *International Journal of Thermophysics* 32 (6), pp. 1111–1124.

10 Supporting Information

Mercury Injection Capillary Pressure (MICP) Measurements

A Micrometrics Autopore IV 9500 Porosimeter was used to precisely measure the amount of mercury injected into the rock samples. After the sample was cleaned, dried and weighted, the appropriate penetrometer was selected and the sample was placed inside the MICP rig. Then, the rig assembly was loaded into the low-pressure chamber of the apparatus. The penetrometer was evacuated to a pressure of less than 0.0009 psia, and filled with mercury at a pressure of 0.5 psia. The bulk volume of the sample was determined at this point. The injection pressure of mercury into the rock sample increased incrementally from 0.5 to 30 psia. After equilibrium was established at the last step (i.e., 30 psia), the injection pressure was reduced to atmospheric pressure, and the penetrometer was removed. The penetrometer was then loaded into the high-pressure chamber of the Autopore system. The mercury was injected into the core plug at increasing incremental pressures (up to 60,000 psia). At each pressure point, mercury intrusion was monitored, while the pressure was held constant. Equilibrium was identified when the rate of intrusion dropped below 0.001 µL/g-sec. Finally, mercury saturations were calculated as a percentage of the pore volume at each pressure. The pore volume used for calculation of mercury saturation was obtained from the maximum intrusion volume of mercury. In the following, the procedure for the determination of pore size distribution by means of MIP experiments is described [1,2].
Firstly, a graph of the fraction of pore volume injected (v) versus pore access radius (r) can be constructed, and the differential of this gives a pore throat size distribution (PSD) function:

$$\mathrm{PSD} = \frac{\mathrm{dv}}{\mathrm{dlog(r)}} \tag{6}$$

The differential is calculated numerically. The central difference method is used to calculate PSD as:

$$\mathrm{PSD}_i = \frac{\mathrm{v}_{i+1} - \mathrm{v}_{i-1}}{\log(\mathrm{r}_{i+1}) - \log(\mathrm{r}_{i-1})} \tag{7}$$

PSD is smoothed using Eq. 8:

$$\mathrm{PSD_i} = \frac{\mathrm{PSD_{i-1}} + 2\mathrm{PSD_i} + \mathrm{PSD_{i+1}}}{4} \tag{8}$$

After that the PSD is normalized to 1 as follows:

$$\mathrm{PSD_{normal\ i}} = \frac{\mathrm{PSD_i}}{\mathrm{PSD_{max}}} \tag{9}$$

Finally, the normalized PSD is presented in the graphical form. Furthermore, based on the mercury capillary pressure–saturation curves and Laplace equation, one can obtain volume fraction–size distributions. The size of corresponding pores (r), idealized as capillary tubes, is obtained from Laplace equation and the saturation change provides the volume fraction of the associated pores. The standard Laplace's law, in which is the surface tension (γ) and is the contact angle (θ), reads as follows:

$$\mathrm{r} = \frac{2\gamma\cos\theta}{P_c} \tag{10}$$

Gas-Brine Capillary Pressure Measurement (Centrifuge Method)

The centrifuge method consists of measuring average fluid saturation versus capillary pressure (P_c) of a sample at hydrostatic equilibrium during rotation at various angular velocities (ω). The sample is initially filled with a fluid and spun within a second fluid at speeds of up to 13,000 rpm). Due to the rotation, the inner fluid is forced out of the sample. The average saturation of a sample can be determined at different rotational speeds by collecting and measuring the volume of produced fluid.

Hassler and Brunner [3], in 1945, were the first to analyze data from centrifuge experiments. They considered four assumptions for their calculations as follows:

- Capillary pressure at the outlet face of the core plug is zero.
- The rock sample is homogeneous.
- The effect of gravitational acceleration is small compared to the centrifugal field.
- The radial character of the centrifugal field is neglected.

According to Hassler and Brunner, at hydrostatic equilibrium, the capillary pressure at any position is equivalent to the difference in hydrostatic pressure between the two phases. Taking the linear variation of the centrifugal field with the distance from the axis of rotation into account, capillary pressure P_c for drainage is given by:

$$P_{c1} = \frac{1}{2}\Delta\rho\omega^2(r_2^2 - r_1^2) \tag{11}$$

where $\Delta\rho$ is the density difference between the two phases (kg/m^3) and r_1 , r_2 are distances to the center of rotation from the inlet and the outlet faces of the plug (m), respectively (as shown in Fig. S1).

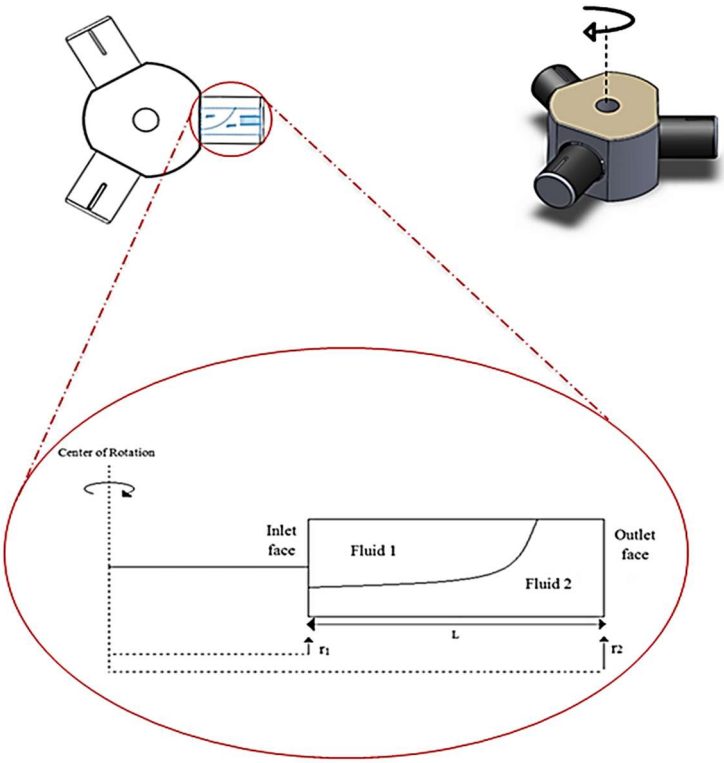

Fig. S1 Schematic diagram of a core plug in a centrifuge and its boundary conditions

Centrifuge Capillary Pressure Test procedure

1) A brine saturated core plug was placed in a core chamber surrounded by the lower density non-wetting fluid (i.e., the gas phase), and then the entire assembly was placed in the rotor of the centrifuge.
2) The first rotational speed was initiated. Due to the centrifugal forces, the denser fluid (i.e., brine) was expelled from the outer end-face of the plug, and the gas phase enters from the inner radial end-face. Brine will be produced from the sample until the centrifugal and capillary forces reach an equilibrium. Meanwhile, the produced brine from the core sample was collected in the graduated tube.
3) Step 2 was repeated for each subsequent rotational speed.

The test runs in minimum eight different incremental rotational speeds (rpm). At each speed, the volume of displaced brine was monitored until no more brine extracted. Generally, equilibrium is reached when no further production is observed. Having the volume of produced brine at each pressure step, the average brine saturation can be calculated using the following equation:

$$\overline{S_w} = \frac{V_p - V_d}{V_p} \tag{12}$$

Where $\overline{S_w}$ is the average brine saturation into the core plug, and V_p and V_d are the pore volume of the plug (cc) and the displaced brine volume (cc) from the core plug.

Table S1 Bulk mineral composition of each sample as determined by XRD analysis.

Sample No. / Mineral (wt%)	Sandstone 1	Sandstone 2	Carbonate 1
Quartz	83.2	76.4	4.7
Calcite	6.0	0.2	43.2
Orthoclase	3.6	4.1	0
Albite	2.1	5.2	0.4
Gypsum	2.9	1.3	18.9
Microcline	1.2	5	1.2
Dolomite	0.1	5.1	25.4
Illite	0.2	1.1	3.7
Barite	0.1	0.2	0
Muscovite	0.4	0.6	0
Chamosite	0.1	0.5	0
Pyrite	0.1	0.2	0.9
Kaolinite	0	0.1	1.6

Table S2 Simulated parameters of Modified Corey model

Exp. No.	$K_{r,\,max}$ [brine]	A [brine]	H [brine]	V [brine]	$K_{r,\,max}$ [gas]	A [gas]	H [gas]	V [gas]
1	1	10.053	0.0191	19.16	0.50	2.719	0.0012	3.11
2	1	10.068	0.0142	15.45	0.35	5.598	0.2100	4.65
3	1	16.000	0.0280	2.00	0.34	13.710	0.8250	3.90
4	1	10.860	0.0000	5.75	0.28	7.200	0.6500	2.50
5	1	6.710	0.0100	10.52	0.26	1.710	0.0700	1.66
6	1	25.274	0.1013	2.00	0.22	57.290	0.5451	30.00
7	1	4.380	0.0100	7.05	0.17	5.020	0.4500	4.00
8	1	5.000	0.0080	9.50	0.17	3.500	0.6000	2.00
9	1	6.710	0.0100	10.52	0.14	1.860	1.6000	1.50

References

(1) Rezaei, A.; Abdollahi, H.; Derikvand, Z.; Hemmati-Sarapardeh, A.; Mosavi, A.; Nabipour, N. Insights into the Effects of Pore Size Distribution on the Flowing Behavior of Carbonate Rocks: Linking a Nano-Based Enhanced Oil Recovery Method to Rock Typing. *Nanomaterials* 2020, *10* (5), 972.

(2) Razavifar, M.; Mukhametdinova, A.; Nikooee, E.; Burukhin, A.; Rezaei, A.; Cheremisin, A.; Riazi, M. Rock Porous Structure Characterization: A Critical Assessment of Various State-of-the-Art Techniques. *Transp. Porous Media* 2021, *136* (2), 431–456.

(3) Hassler, G. L.; Brunner, E. Measurement of Capillary Pressures in Small Core Samples. *Trans. AIME* 1945, *160* (01), 114–123.